ARL-TR-9727 ● JULY 2023

Euler Solution–Generated Database for a High-Speed Guided Projectile

by Justin Paul

NOTICES

Disclaimers

The findings in this report are not to be construed as an official Department of the Army position unless so designated by other authorized documents.

Citation of manufacturer's or trade names does not constitute an official endorsement or approval of the use thereof.

Destroy this report when it is no longer needed. Do not return it to the originator.

ARL-TR-9727 ● JULY 2023

Euler Solution–Generated Database for a High-Speed Guided Projectile

Justin Paul
DEVCOM Army Research Laboratory

REPORT DOCUMENTATION PAGE

1. REPORT DATE	2. REPORT TYPE	3. DATES COVERED	
		START DATE	END DATE
July 2023	Technical Report	1 January 2020	31 August 2022

4. TITLE AND SUBTITLE
Euler Solution–Generated Database for a High-Speed Guided Projectile

5a. CONTRACT NUMBER	5b. GRANT NUMBER	5c. PROGRAM ELEMENT NUMBER
5d. PROJECT NUMBER	**5e. TASK NUMBER**	**5f. WORK UNIT NUMBER**

6. AUTHOR(S)
Justin Paul

7. PERFORMING ORGANIZATION NAME(S) AND ADDRESS(ES)	8. PERFORMING ORGANIZATION REPORT NUMBER
DEVCOM Army Research Laboratory ATTN: FCDD-RLA-WD Aberdeen Proving Ground, MD 21005	ARL-TR-9727

9. SPONSORING/MONITORING AGENCY NAME(S) AND ADDRESS(ES)	10. SPONSOR/MONITOR'S ACRONYM(S)	11. SPONSOR/MONITOR'S REPORT NUMBER(S)

12. DISTRIBUTION/AVAILABILITY STATEMENT
DISTRIBUTION STATEMENT A. Approved for public release: distribution unlimited.

13. SUPPLEMENTARY NOTES
ORCID ID: Justin Paul, 0000-0003-4133-7585

14. ABSTRACT
This investigation documents the generation of an inviscid aerodynamic database for a high-speed guided projectile. The database was generated using the Cart3D inviscid computational fluid dynamics solver. The characteristics of this database are primarily depicted in this report as surface plots showing a variety of perspectives with commentary providing additional insight and rationale for the shape and behavior of trends in the data. Fitting techniques were used for interpolation and, in rare cases, extrapolation to fill in a small percentage of anomalous data in the database. In addition to documenting the characteristics of the database, more insights and context for the roll-dependent aerodynamics of this projectile are provided as complementary to previous reports on such subject matter. As expected, the inviscid database exhibited decreasing aerodynamic coefficient magnitude with increasing Mach number and increasing normal force coefficient and pitching moment coefficient with increasing total angle of attack. Sinusoidal roll reversal in rolling moment coefficient was also observed with increasing Mach number. Finally, comparisons of the inviscid database are plotted against more sophisticated methods of evaluating the aerodynamic performance to evaluate the accuracy of the database.

15. SUBJECT TERMS
long-range guided projectiles, computational fluid dynamics, aerodynamic characterization, Cart3D, Weapons Sciences

16. SECURITY CLASSIFICATION OF:			17. LIMITATION OF ABSTRACT	18. NUMBER OF PAGES
a. REPORT	b. ABSTRACT	C. THIS PAGE		
UNCLASSIFIED	UNCLASSIFIED	UNCLASSIFIED	UU	54

19a. NAME OF RESPONSIBLE PERSON	19b. PHONE NUMBER *(Include area code)*
Justin Paul	(410) 306-0797

STANDARD FORM 298 (REV. 5/2020)
Prescribed by ANSI Std. Z39.18

Contents

List of Figures

List of Tables

1. Introduction

Full characterization of a projectile can be difficult because the aerodynamics can be sufficiently complicated as to necessitate high fidelity simulations and experimental data while the design space may be multi-modal and large enough to render a brute force approach prohibitively expensive. Efforts have been made to resolve this issue by evaluating different aeroprediction methodologies to assess their respective strengths and weaknesses as well as using data fusion techniques to apply aeroprediction methodologies of varying fidelity together while leveraging their complementary strengths, thus cutting down on cost.[1,2]

A generic high-speed projectile designed for long-range flight has been the subject of extensive investigation and analysis being featured in numerous reports and with different theses including shape optimization and design,[3,4] aeroprediction method comparisons,[1] roll dependency aerodynamic analysis,[2,5,6] experimental and simulation-based data set generation and aerodynamic modeling construction.[2,7–9]

The primary purpose of this report is to document the inviscid aerodynamic database generated for this generic, high-speed, long-range projectile. The secondary purpose is to provide additional context for the roll-dependent aerodynamics in this featured inviscid aerodynamic database.[1-4,6–9] These primary and secondary purposes serve in support of the significant focus that has been placed on analyzing this projectile. The tertiary purpose of this report is to provide comparison of this inviscid database with experimental and higher-fidelity computational aerodynamic characterization analyses.

2. Projectile Description

The test projectile is a baseline geometry that was shaped through a series of optimization analyses that identified design candidates with low drag and high lift-to-drag ratios while maintaining marginal stability across the supersonic Mach regime.[10] Figure 1 and Table 1 present the projectile characteristics. The body is 10 calibers (cal.) in length with an 0.5 cal. long, 7° boattail and has a center of gravity located at 6.0 cal. from the nose. The projectile has a 3-cal. long ogive, with a 0.1 cal. radius-rounded nose tip. There are four low-aspect-ratio, clipped-delta fins arrayed symmetrically around the body with a total fin span of 1.93 cal. Control is provided using movable trailing edge flaps on each of the four fins, which are rotated about their one-half chord location. These control surfaces are sized at 80-mm chord to provide sufficient control authority to execute desired maneuvers.[9]

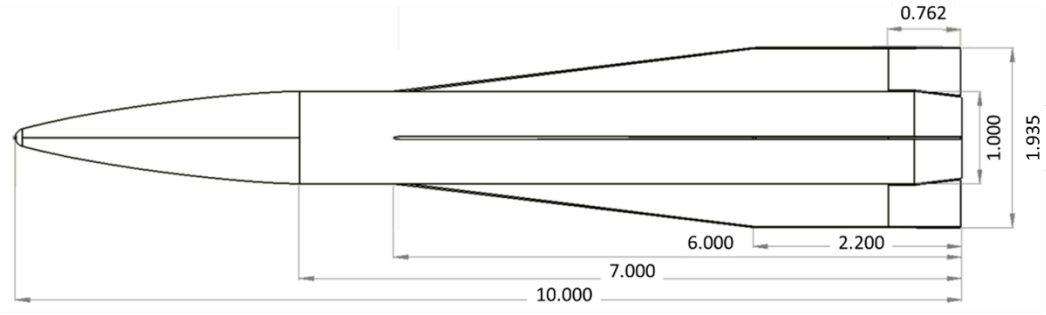

Fig. 1 Generic high-speed projectile geometry (dimensioned in calibers)

Table 1 Parameters of the generic high-speed projectile

Diameter (mm)	Length-to-diameter	Ogive length of OAL	Root fin chord (cal.)	Tip fin chord (cal.)	Fin span (cal.)
105	10	0.3	6	2.2	1.935

3. Data Generation Methodology

The data was generated from simulations ran using a software package called Cart3D developed by the National Aeronautics and Space Administration (NASA). NASA's Cart3D is an inviscid computational fluid dynamics (CFD) package for aerodynamic design and analysis. Cart3D provides utility for surface modeling and intersection, mesh generation, flow simulation, and postprocessing.[11] The mesh generation software with the Cart3D package produces Cartesian meshes for arbitrarily complex, watertight geometries. The mesh generation process automatically increases the fidelity of the domain near small features and curvature present in the geometry to better resolve flow features near the surface. The meshes generated for the simulations numbered approximately 6.1 million cells. This was the result of using 14 levels of refinement in a cartesian computational domain with an inscribed sphere of 14 body lengths. The meshes were also further refined using prescribed density boxes near the nose and near the body of the geometry. An example of one of the meshes is shown in Fig. 2. Aerodynamic coefficients for a given flight condition (i.e., Mach number [M_∞] and aerodynamic angles) are computed in several minutes by the flow solver called "flowCart," which will be the designation for Cart3D data in comparison to other data sources in this report.

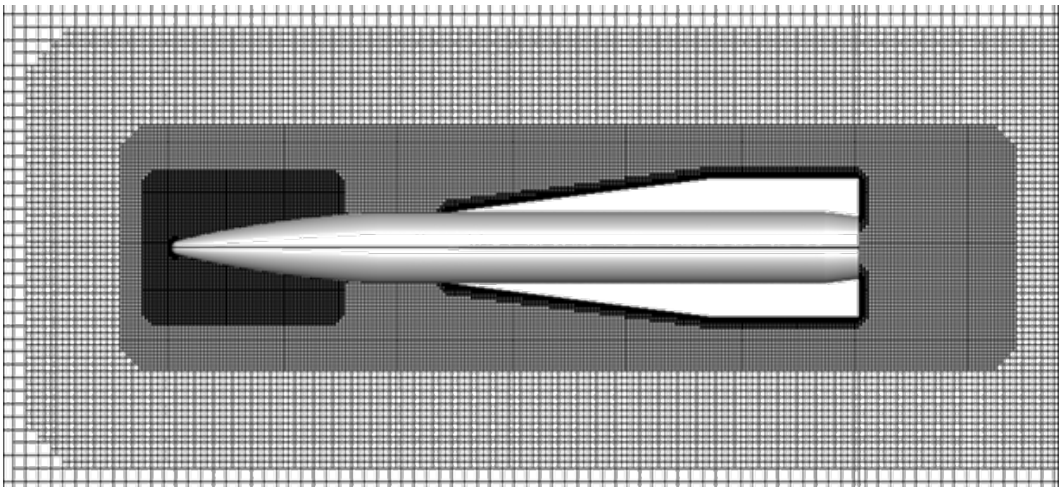

Fig. 2 View of an example Cart3D mesh

For all simulations, the geometry was oriented in the "+" configuration in the mesh with the only one deflectable flap set on the starboard side. This orientation characterizes the zero roll orientation (ϕ = 0°). For additional reference and clarification, a visualization of the vehicle in three different roll orientations is shown in Fig. 3. Positive deflection of the flap corresponds to counterclockwise rotation as viewed from the starboard side while negative flap deflection is the opposite rotation. This is best illustrated in Fig. 4.

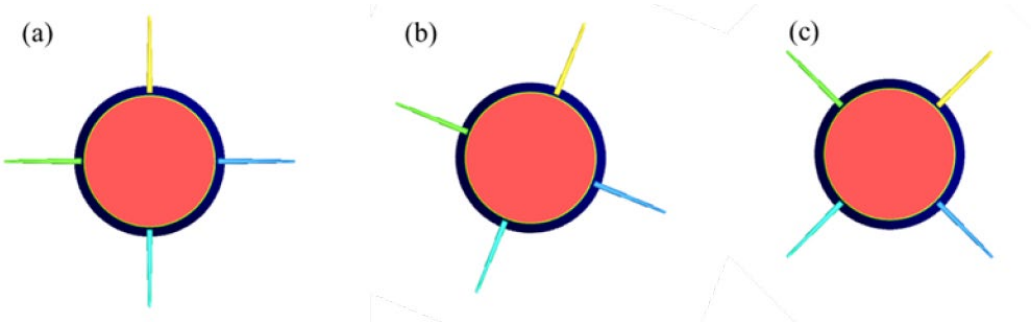

Fig. 3 Example roll (ϕ) orientations at ϕ = 0° (a), ϕ = 22.5° (b), ϕ = 45° (c)

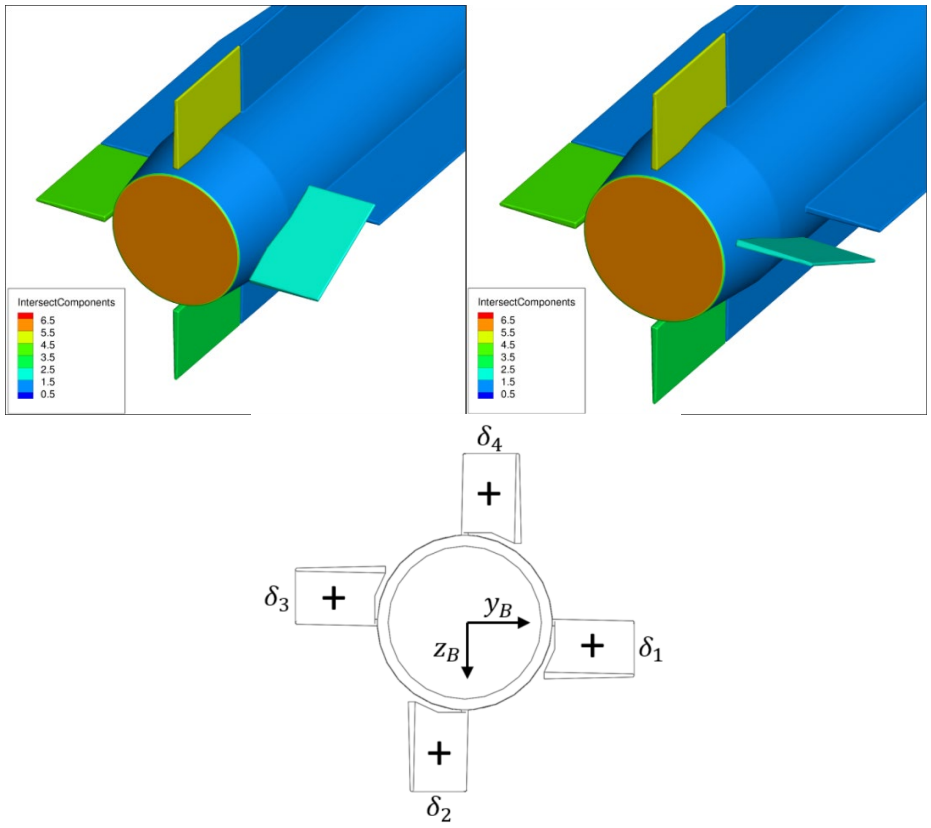

Fig. 4 Positive flap deflection, δ = 25° (top left), negative flap deflection, δ = –25° (top right), and flap numbering system (bottom)

Since each of the four flaps can be independently deflected, a full aerodynamic characterization of the projectile for each individual flap would have been prohibitively expensive in both computational energy cost and time. For this reason, a one-flap deflection characterization approach was chosen that requires less than 93,000 individual simulations. The calculation of total simulations required is explained later. The rationale of using the one-flap approach to achieve the same aerodynamic characterization of the full aerodynamic characterization of the projectile is using a component-based force and moment decomposition of the projectile. Once this is accomplished, the component forces and moments can then be "built-up" to reconstruct the forces and moments acting on the entire projectile. The linear relationship of forces acting on all the components enables leveraging the superposition principle.[12] Therefore, the aerodynamics of the projectile can be reconstructed for a given Mach number, total angle of attack, and roll angle with any configuration of flap deflection for each of the individual four flaps.

Different flow conditions were simulated using a relative wind vector parameterized by Mach number, roll angle (ϕ), and total angle of attack (α_T). An example of the relative wind vector is shown in Fig. 5. Due to the construction and programming of Cart3D, roll angle and total angle of attack need to be converted into angle of attack (α) and side slip angle (β) using Eqs. 1 and 2.

$$\alpha = \tan^{-1}(\tan(\alpha_T) * \cos(\phi)) \tag{1}$$

$$\beta = \sin^{-1}(\sin(\alpha_T) * \sin(\phi)) \tag{2}$$

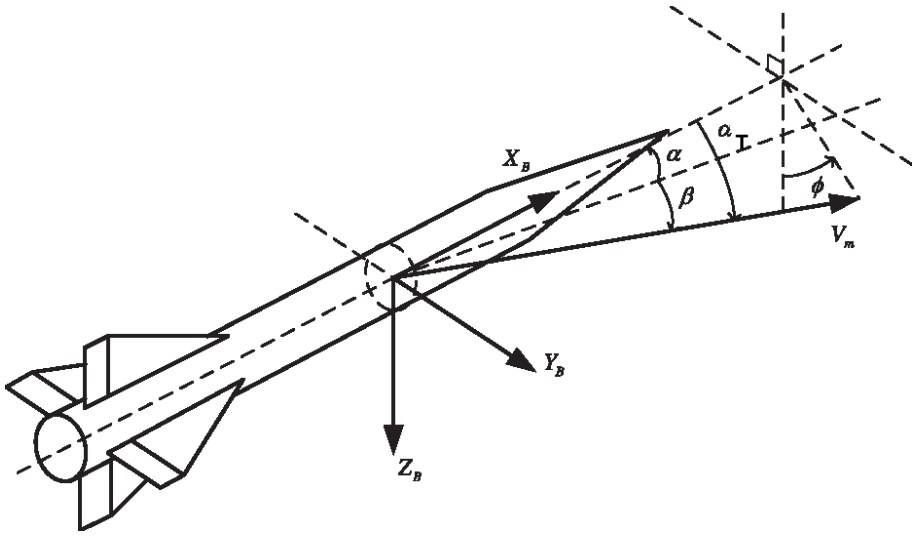

Fig. 5 Example of a relative wind vector for a generic projectile characterized by [α, β], or [α_T, ϕ]

Including the flap deflection angle, the full simulation matrix defining the dimensions of the inviscid aerodynamic database is defined by 12 α_T, 15 δ, 16 M_∞, and 32 ϕ. This simulation matrix yields a total quantity of 92,160 unique simulations. Figure 6 serves to better illustrate the size and complexity of this simulation matrix. Due to this large number of simulations, an in-house python driver system was used to automate job control and data logistics. The total project cost approximately 650,000 compute hours on the high performance computing machine Onyx at the US Army Engineer Research and Development Center Department of Defense Supercomputing Resource Center.

Flap Deflection (15)	Mach (16)
	Subsonic: {0.45,0.55,0.65}
	Transonic:{0.75,0.85,0.95,1.02}
0°	Supersonic: {1.2,1.5,2.0,2.5,3.0,3.5,4.0}
±2°	
±5°	Hypersonic: {6.0,9.0}
±10°	**Total Angle of Attack (12)**
±15°	{0,2,4,6}°
±20°	{8,10,12}°
±25°	{14,18,20}°
±30°	{25}°

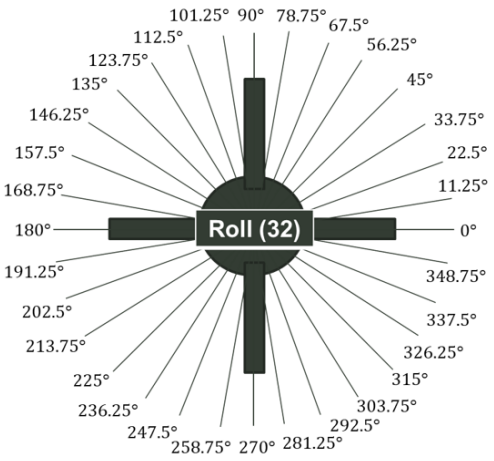

Total of 92160 cases

Fig. 6 Quantity and values of parameters defining the simulation matrix

Some final notes on displaying this data are steps that were taken to postprocess the data for visualization. One issue with this database that was noticed only after the simulations were completed (the simulations were completed much faster than they could be analyzed), was the existence of certain "anomalous" data points. In certain cases, these anomalous data points were obvious in the sense that the normal force coefficient (C_N) was recorded as $-1.5e^{120}$. Unfortunately, in other cases, anomalous data points are a little more subtle in the sense that C_N was recorded as 56, where it is clear from trends in the rest of the database that C_N in this particular context should be much lower with bounds of 5 and 15. There are even cases where anomalous data points are so subtle their deviation from an "expected" value would only be discovered upon close inspection. Compounding this issue is the fact that some anomalous data points can exist right next to each other across multiple dimensions in the database. Fortunately, this issue is somewhat small. A quick survey of the database yields only 0.591% of simulations with aerodynamic coefficients that lie outside the bounds of –40 and 40. There are still a small quantity of anomalous data points that lie inside these bounds but they are also amenable to rectification through inference of interpolation and in rare cases even extrapolation. Once the most extreme anomalous data points are excluded, there are also certain mathematical descriptions that can be used to characterize the database that match well with the raw database itself as well as other sources of data calculated and estimated to characterize the performance of the projectile.[1,2]

Polynomial regression is a popular regression method and is especially effective when the data is expected to conform to a particular polynomial function. Polynomials are modeled by Eq. 3 where the "degree" of the polynomial is

characterized by the number n. The derivative of the polynomial model is given by Eq. 4.

$$y = \xi_0 x^0 + \xi_1 x^1 + \xi_2 x^2 + \cdots + \xi_n x^n \tag{3}$$

$$\frac{dy}{dx} = 1\xi_1 x^0 + 2\xi_2 x^1 + 3\xi_2 x^2 \ldots + n\xi_n x^{n-1} \tag{4}$$

The process of fitting this model to an arbitrary data set is fairly straightforward, where infinitesimal changes in x produce an effect on y by way of the derivative of the function shown in Eq. 4. The only caveat is that the "degree" of the polynomial must be of order $n - 1$ for the polynomial to be unique. In order to accomplish this, the built-in MATLAB function polyfit was used, which has the syntax of Eq. 5 where x and y are the coordinates for the arbitrary data set and n is the degree of the polynomial. The result, p, is then the model of the polynomial (coefficients, residuals, etc.). An example of implementing the polyfit function is shown in Fig. 7.

$$p = polyfit(x, y, n) \tag{5}$$

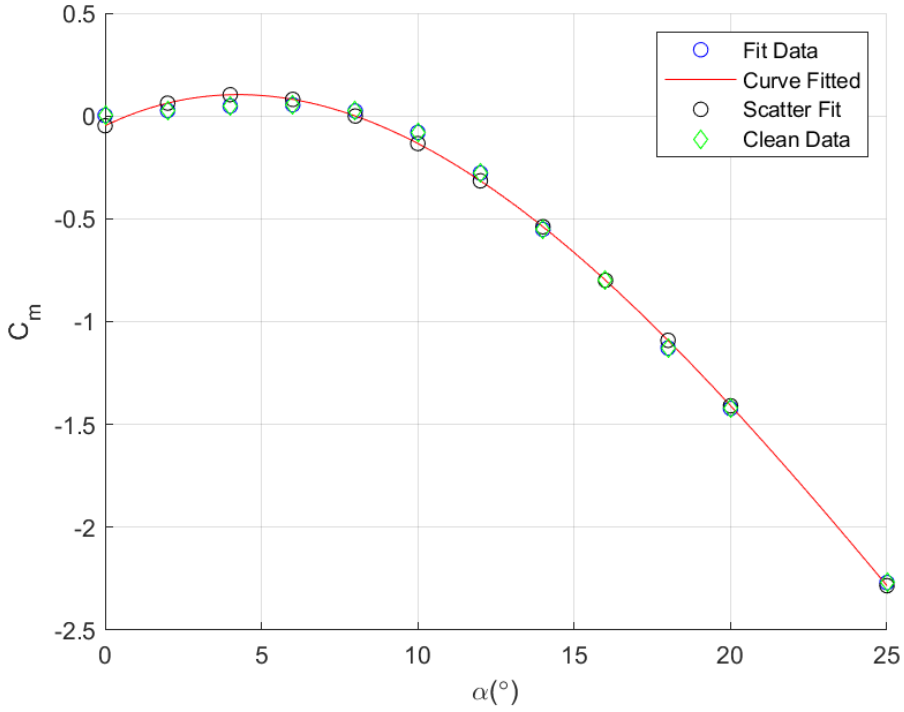

Fig. 7 Example of cubic polynomial fitting of pitching moment coefficient (C_m) at $M_\infty = 9$ for $\phi = 315°$ and $\delta = 5°$

The ambiguity of the labels in the legend of Fig. 7 warrant explanation. The "Fit Data" are the raw data pulled from the database that are useful for generating the fit (this excludes the anomalous data). The "Curve Fitted" data is the regression function generated using the "Fit Data." The "Scatter Fit" data is the data generated by the "Curve Fitted" function at the same total angle of attack or roll angle as each point in the "Fit Data." Finally, the "Clean Data" is the merger of "Fit Data" and "Scatter Fit" data prioritizing "Fit Data" where it makes sense and using "Scatter Fit" data where anomalous data exists.

Regression by way of Fourier analysis is also a popular regression method and is useful when the function that needs to be modeled has a somewhat arbitrary relationship to the independent variable. This form of regression is accomplished by using the sums of simpler trigonometric functions to fit the data set. The general form of a Fourier series is shown in Eq. 6.

$$y = a_0 + \sum_{i=1}^{n} a_i \cos(i\omega x) + b_i \sin(i\omega x) \tag{6}$$

The process of fitting this model to an arbitrary data set is slightly different from the more straightforward linear least squares regression procedure, in that it is now nonlinear. The procedure now involves using iterative methods such as Gauss-Newton or Levenberg-Marquardt algorithms and reaching a specified convergence criterion. The objective function these iterative algorithms typically solve has the general form shown in Eq 7.

$$\hat{\psi} \in argmin_{\psi} S(\psi) \equiv argmin_{\psi} \sum_{i=1}^{m} [y_i - f(x_i, \psi)]^2 \tag{7}$$

To accomplish this, the built-in MATLAB function fit with the fit-type option of "fourier8" was used, which indicates 8 pairs (n = 8) of trigonometric functions that have the syntax of Eq. 8 where x and y are the coordinates for the arbitrary data set. The result, F, is then the model of the function (coefficients, confidence bounds, frequency ω, etc.) An example of implementing Fourier regression is shown in Fig. 8.

$$F = fit(x, y, "fourier8") \tag{8}$$

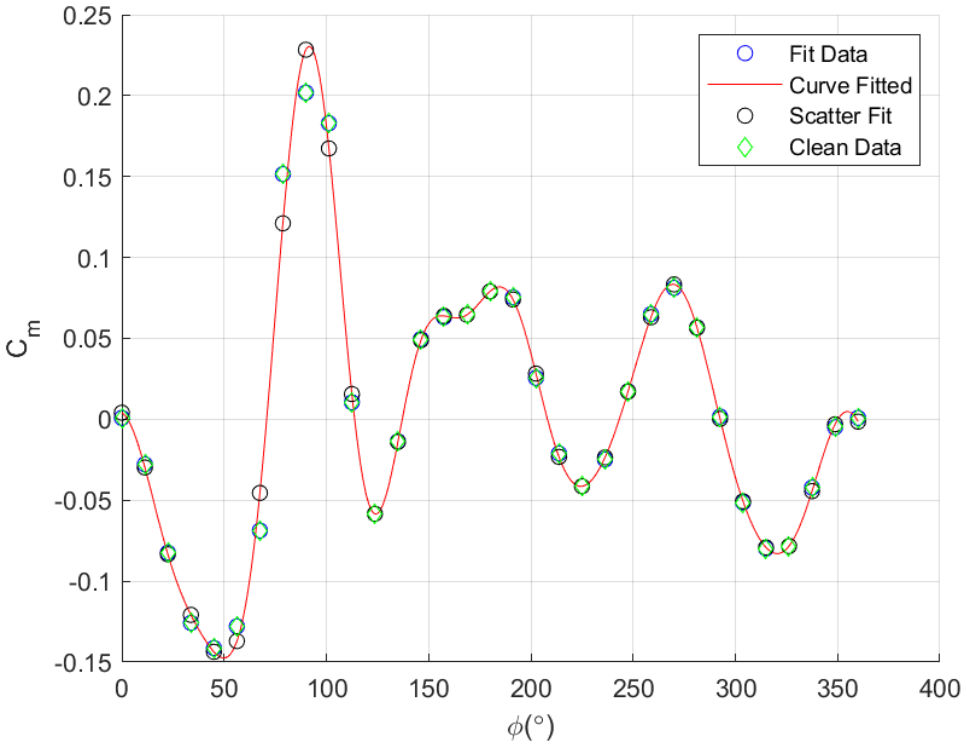

Fig. 8 Example of Fourier fitting of pitching moment coefficient (C_m) at $M_\infty = 9$ for $\alpha_T = 10°$ and $\delta = 5°$

4. Results

4.1 Analyzing C_N and C_m at ϕ = 0° and ϕ = 45°

The natural starting point for documenting the performance of the projectile is analyzing the body frame aerodynamic coefficients at a flap deflection angle of zero degrees (δ = 0°) and the "+" roll orientation (ϕ = 0°). Typical body frame aerodynamic coefficients that are important for performance are C_N and C_m. The surface plot for C_N versus α_T and M_∞ is shown in Fig. 9.

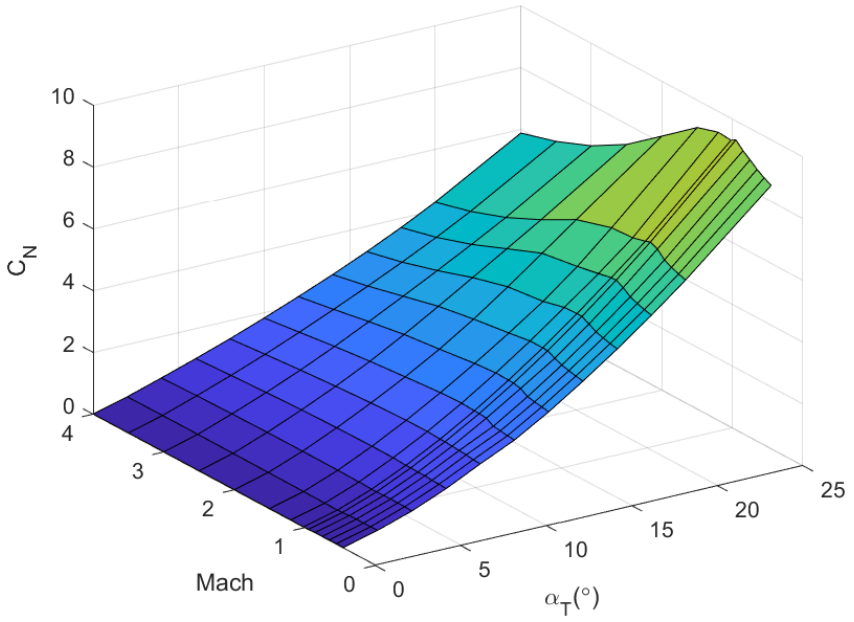

Fig. 9 C_N vs. α_T and M_∞ for δ = 0° and ϕ = 0°

In the surface plot shown in Fig. 9, we observe expected trends. C_N increases with increasing α_T and decreases with increasing M_∞ in the supersonic regime. There is also an expected sharp increase in C_N in the transonic region. In Fig. 10, we see the surface plot for C_m versus α_T and M_∞, which also displays expected trends for a stable projectile. C_m decreases with increasing α_T and increases with increasing M_∞ in the supersonic region. Similar to C_N, there also seems to be a corresponding decrease (but increase in magnitude) in C_m in the transonic region at high α_T .

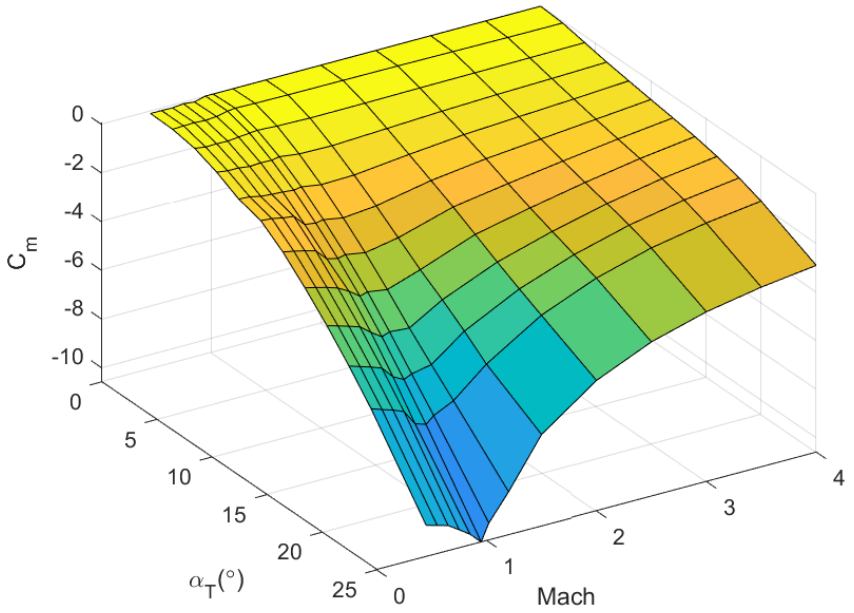

Fig. 10 C_m vs. α_T and M_∞ for $\delta = 0°$ and $\phi = 0°$

We can continue our analysis by also analyzing the corresponding data but at the "x" roll orientation ($\phi = 45°$). The surface plot for C_N versus total angle of attack (α_T) and M_∞ is shown in Fig. 11. The surface plot for C_m versus α_T and M_∞ is shown in Fig. 12.

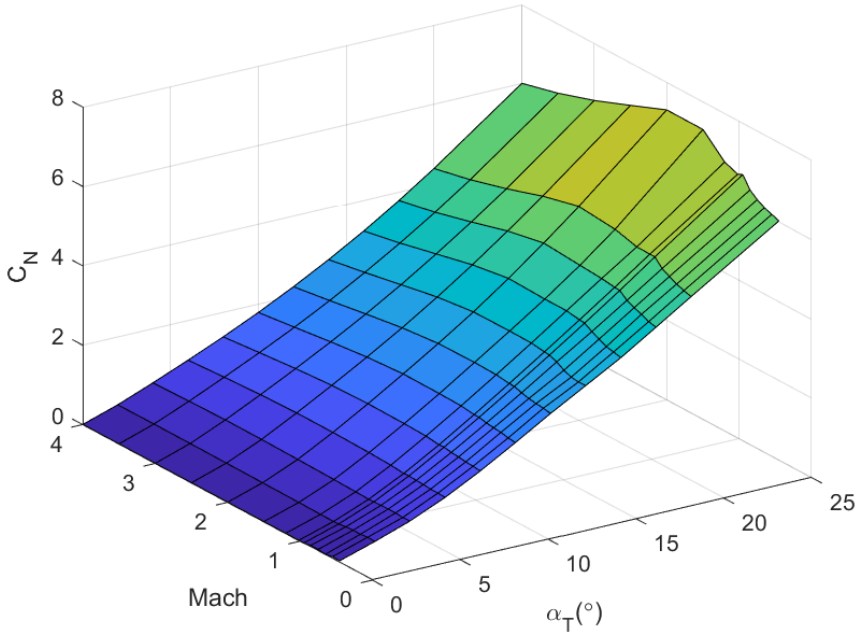

Fig. 11 C_N vs. α_T and M_∞ for $\delta = 0°$ and $\phi = 45°$

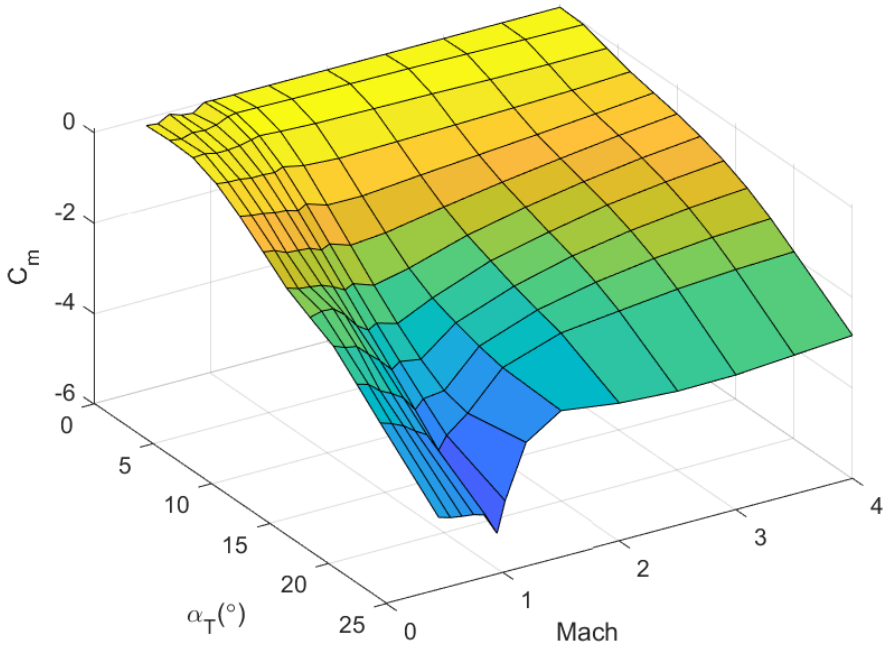

Fig. 12 C_m vs. α_T and M_∞ for δ = 0° and ϕ = 45°

The main difference in C_N comparing "+" roll orientation (ϕ = 0°) and "x" roll orientation (ϕ = 45°) is an overall decrease in magnitude and a relative decrease in the transonic region at high angles of attack. Additionally we see a related difference in C_m as an overall increase (decrease in magnitude). In order to get a better sense of how these differences in C_N and C_m impact the static stability of the projectile, we need to calculate the nondimensional center of pressure relative to the center of gravity. For clarification, in this investigation, x_{cp} is calculated unconventionally as Eq. 9. The surface plot for $x_{cp}^{\phi=0^\circ}$ versus α_T and M_∞ is shown in Fig. 13 while the surface plots for $x_{cp}^{\phi=45^\circ}$ versus α_T M_∞ is shown in Fig. 14. For clarity, we can better understand the comparison to these two surface plots by visualizing Δx_{cp}^{ϕ} directly, which is shown in Fig. 15. The value of Δx_{cp}^{ϕ} is calculated by taking the x_cp value for ϕ = 0° and subtracting the value for ϕ = 45°. This is reiterated in Eq. 10.

$$x_{cp} = \frac{C_m}{C_N} \tag{9}$$

$$\Delta x_{cp}^{\phi} = x_{cp}^{\phi=0^\circ} - x_{cp}^{\phi=45^\circ} \tag{10}$$

Equation 10 means negative Δx_{cp}^{ϕ} values indicate a loss in stability (center of pressure moves forward, closer to center of gravity) while positive Δx_{cp}^{ϕ} values indicate a gain in stability in the "x" roll orientation (ϕ = 45°) from the "+" roll orientation (ϕ = 0°). Figure 15 clearly shows that the "x" roll orientation is less

statically stable at virtually all α_T. This observation is directly related to roll-dependent aerodynamics inherent for this particular projectile.[2,5,6]

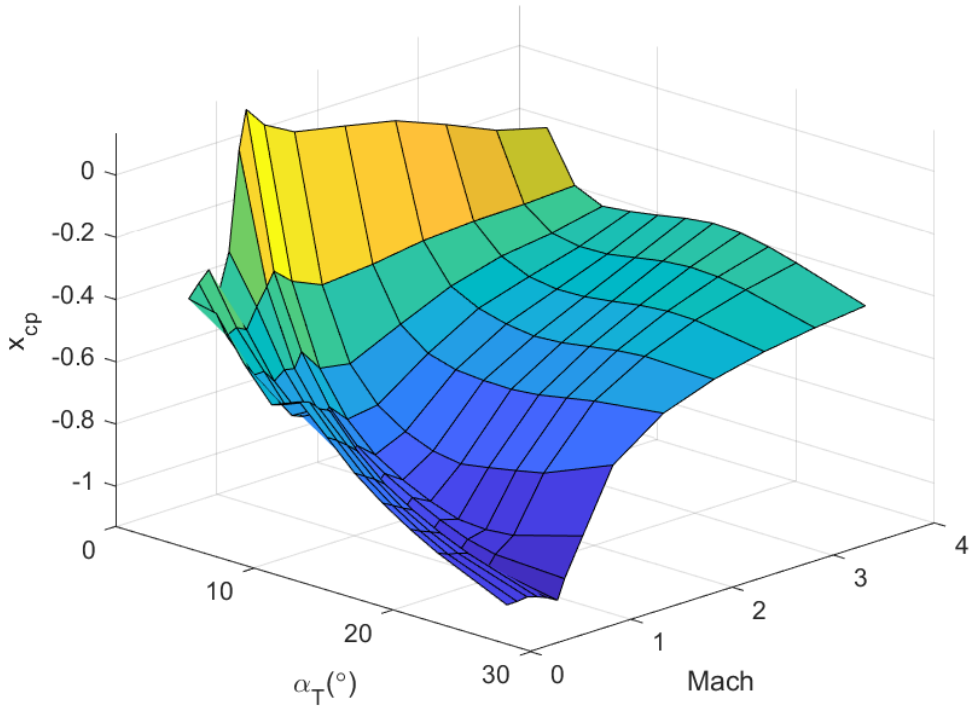

Fig. 13 $x_{cp}^{\phi=0^\circ}$ **vs.** α_T **and** M_∞ **for** $\delta = 0°$

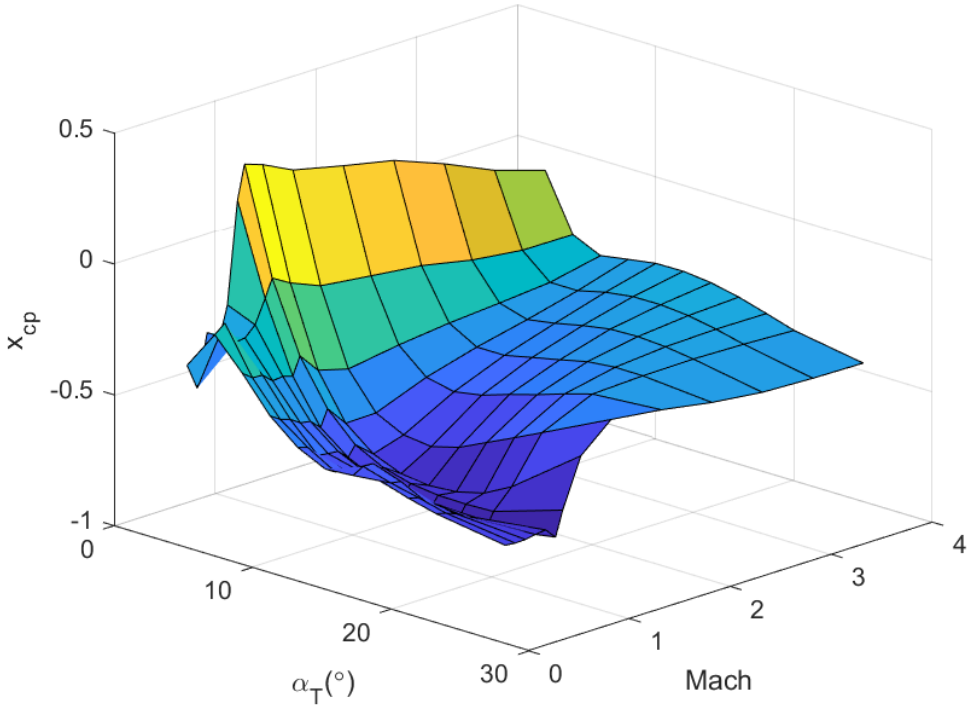

Fig. 14 $x_{cp}^{\phi=45^\circ}$ **vs.** α_T **and** M_∞ **for** $\delta = 0°$

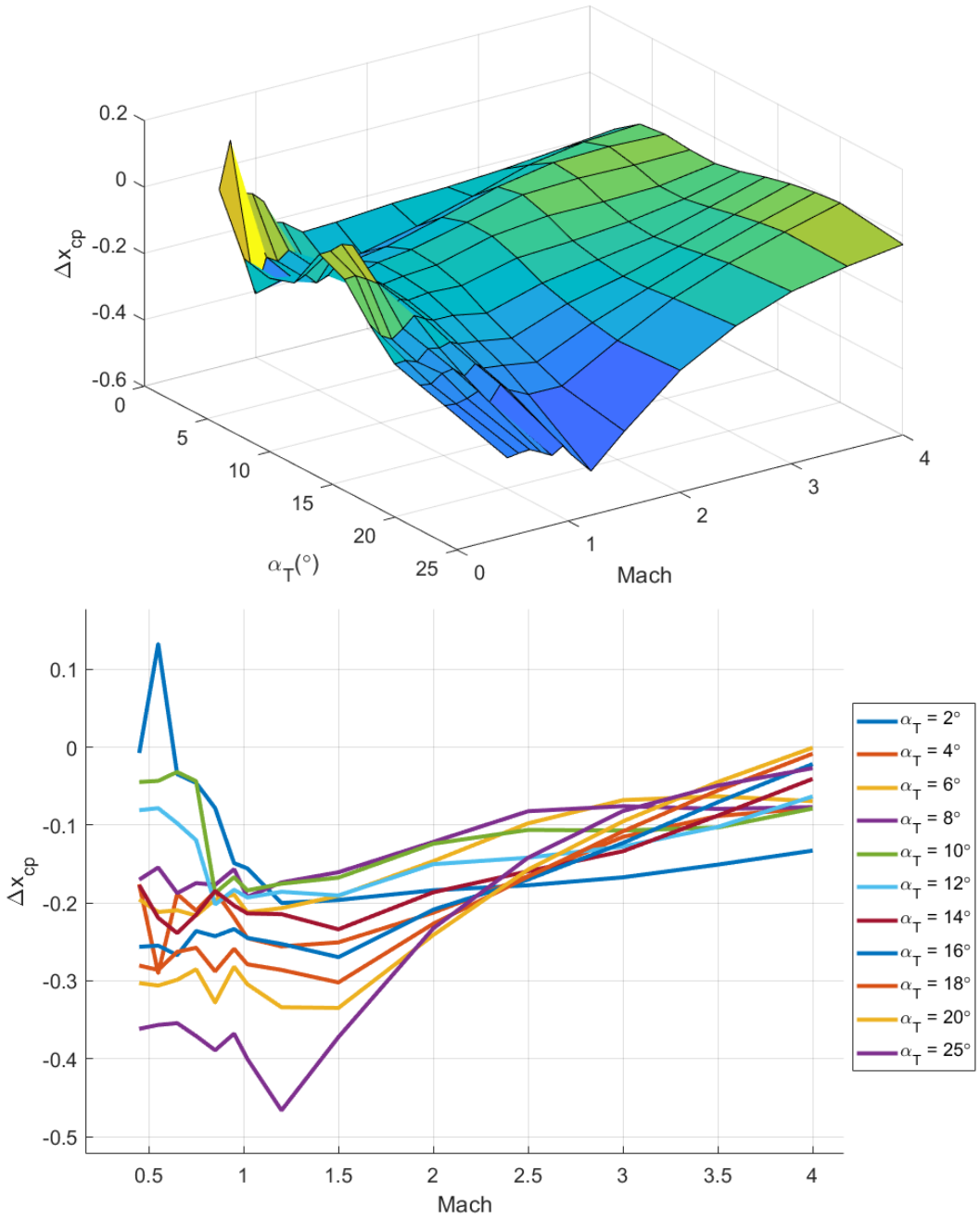

Fig. 15 Δx_{cp}^{ϕ} between ϕ = 0° and ϕ = 45° vs. α_T and M_∞ for δ = 0° (top) and Δx_{cp}^{ϕ} between ϕ = 0° and ϕ = 45° vs. M_∞ for δ = 0° (bottom) calculated from Eq. 10

The surface plots of C_N and C_m at ϕ = 0° and ϕ = 45° for additional flap deflection angles are presented in Figs. 16 and 17. This observation of decreased magnitude of C_N and C_m and thus decreased stability in the "x" roll orientation for this projectile configuration was previously documented.[6] That investigation noted how the windward strakes are more effective than the leeward strakes in the "x" roll orientation, which induces a forward shift of x_{cp}, leading to lowered static stability.

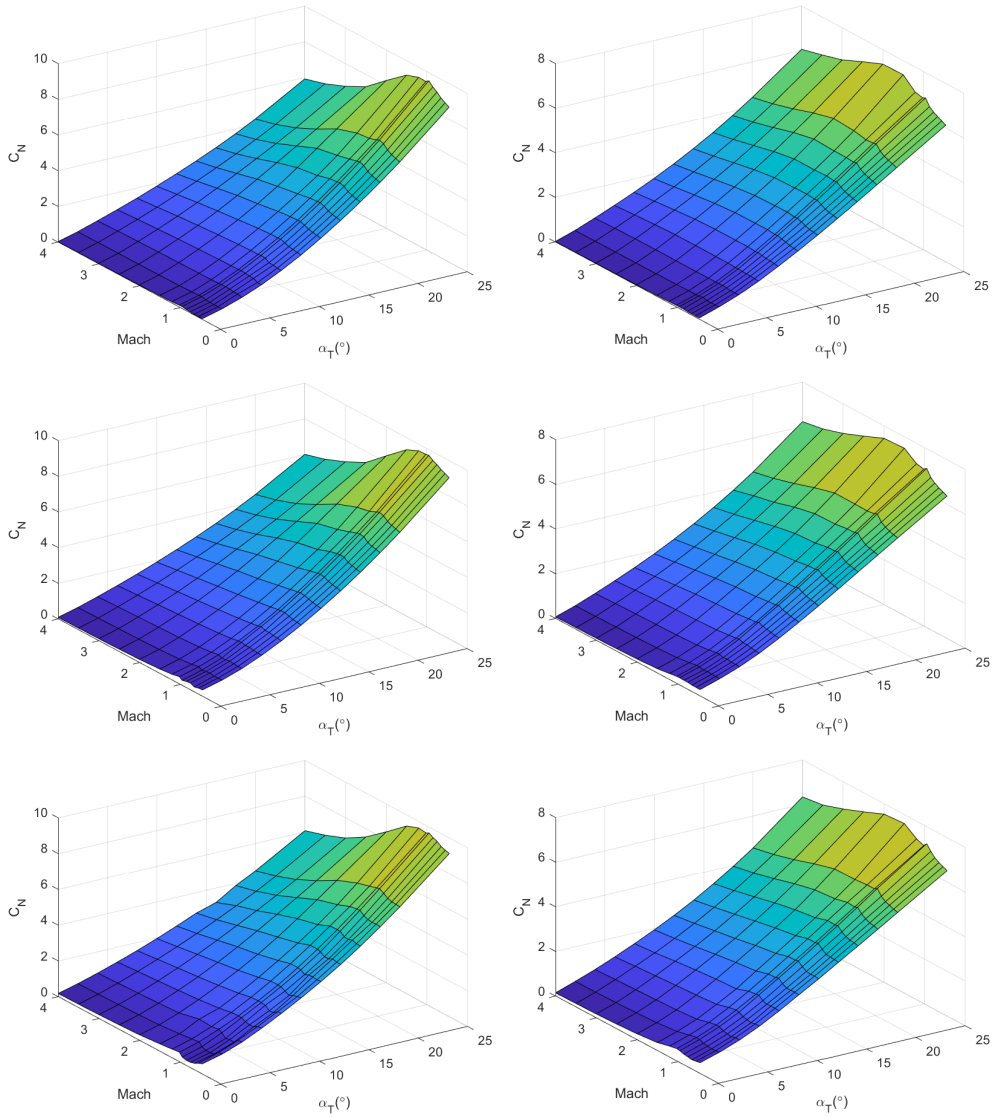

Fig. 16 C_N **vs.** α_T **and** M_∞ **at** ϕ **= 0° (left) and** ϕ **= 45° (right) for** δ **= 5° (top row),** δ **= 15° (middle row), and** δ **= 25° (bottom row)**

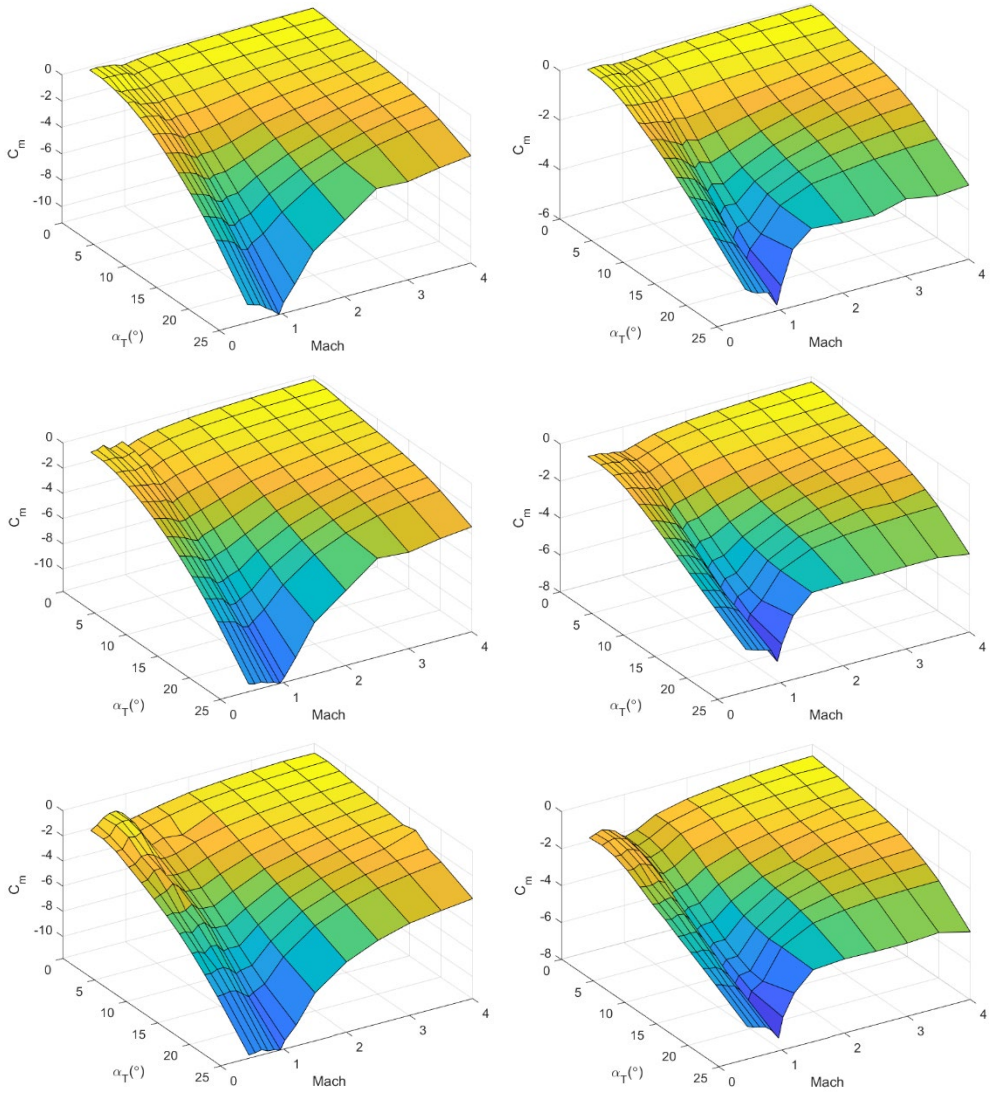

Fig. 17 C_m vs. α_T and M_∞ at ϕ = 0° (left) and ϕ = 45° (right) for δ = 5° (top row), δ = 15° (middle row), and δ = 25° (bottom row)

Now that we have analyzed two particular roll angles across α_T, M_∞, and δ, comparing aerodynamic performance and identifying specific trends and thresholds with their underlying physics, we can use this comparison case to further investigate a full roll sweep of this inviscid aerodynamic database.

4.2 Analyzing C_N and C_m at α_T = 6° and α_T = 16°

Now we compare C_N and C_m versus roll orientation (ϕ) and M_∞ at a given δ and a given α_T. Once again, we can focus on the comparison of these aerodynamic coefficients between two aerodynamic angles just as we compared two roll orientations. Now we will compare two total angles of attack. The two angles chosen for the second comparison are a α_T = 6° and α_T = 16°. At a total angle of

attack at 6 degrees (α_T = 6°) the surface plot for C_N versus ϕ and M_∞ is shown in Fig. 18 and the surface plot for C_m versus ϕ and M_∞ is shown in Fig. 19. At a total angle of attack at 16 degrees (α_T = 16°) the surface plot for C_N versus ϕ and M_∞ is shown in Fig. 20 and the surface plot for C_m versus ϕ and M_∞ is shown in Fig. 21.

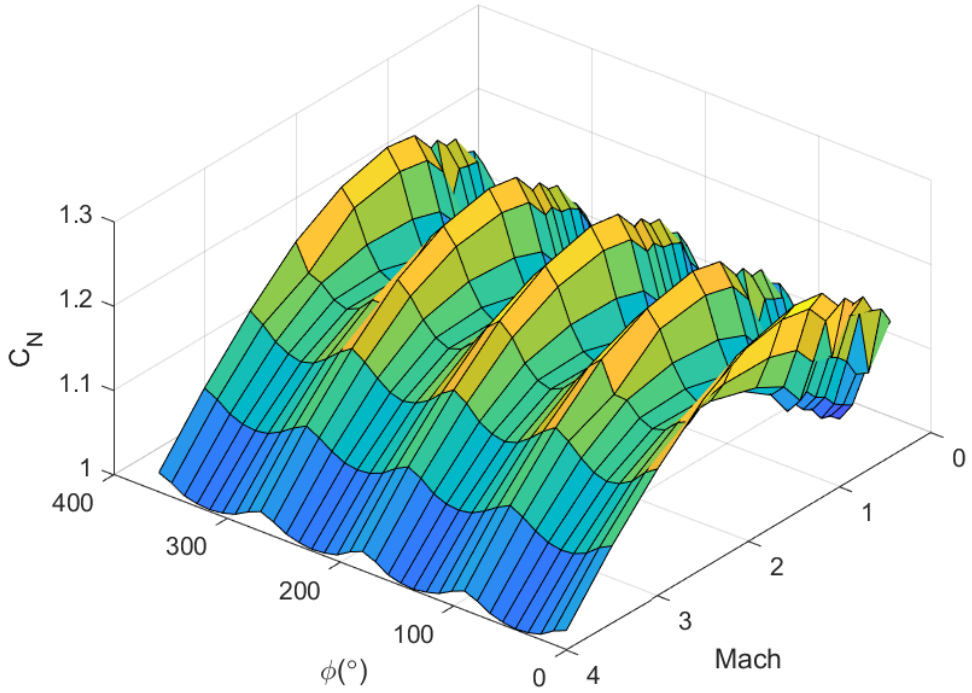

Fig. 18 C_N vs. ϕ and M_∞ for δ = 0° and α_T = 6°

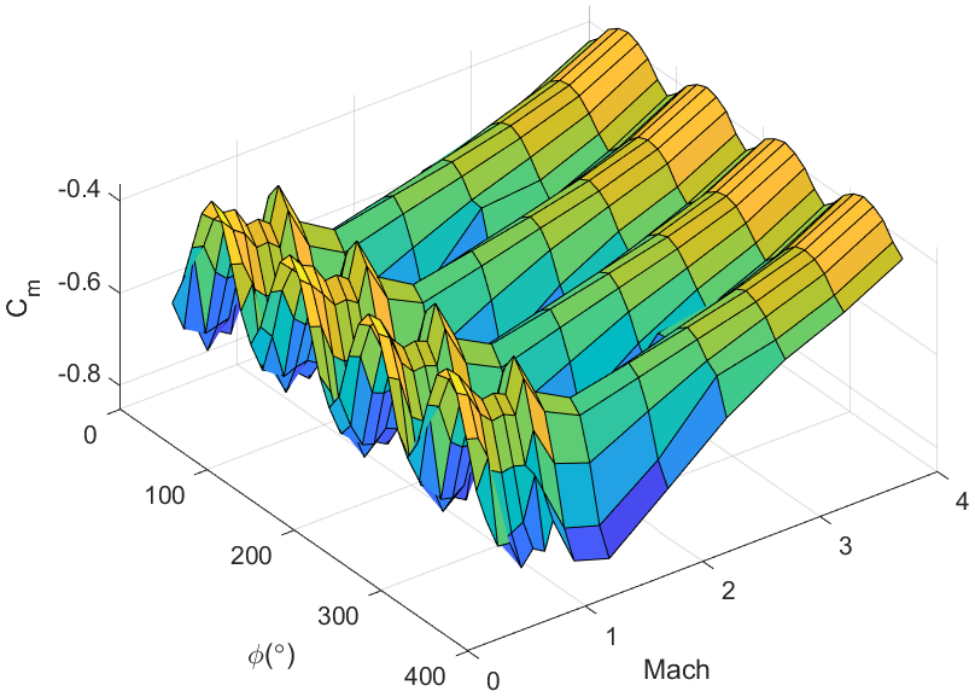

Fig. 19 C_m **vs.** ϕ **and** M_∞ **for** $\delta = 0°$ **and** $\alpha_T = 6°$

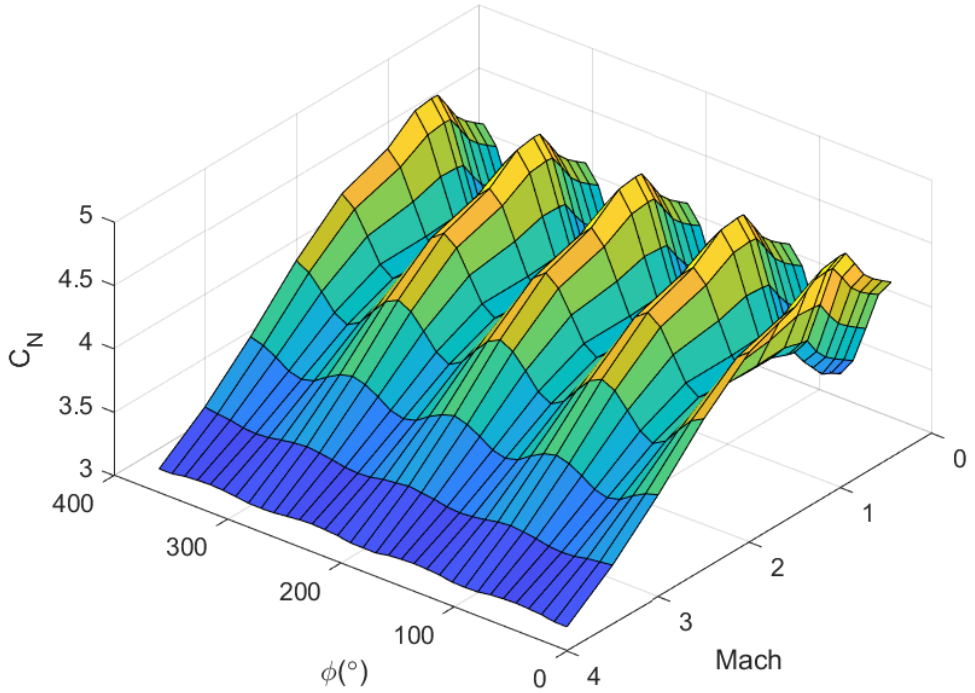

Fig. 20 C_N **vs.** ϕ **and** M_∞ **for** $\delta = 0°$ **and** $\alpha_T = 16°$

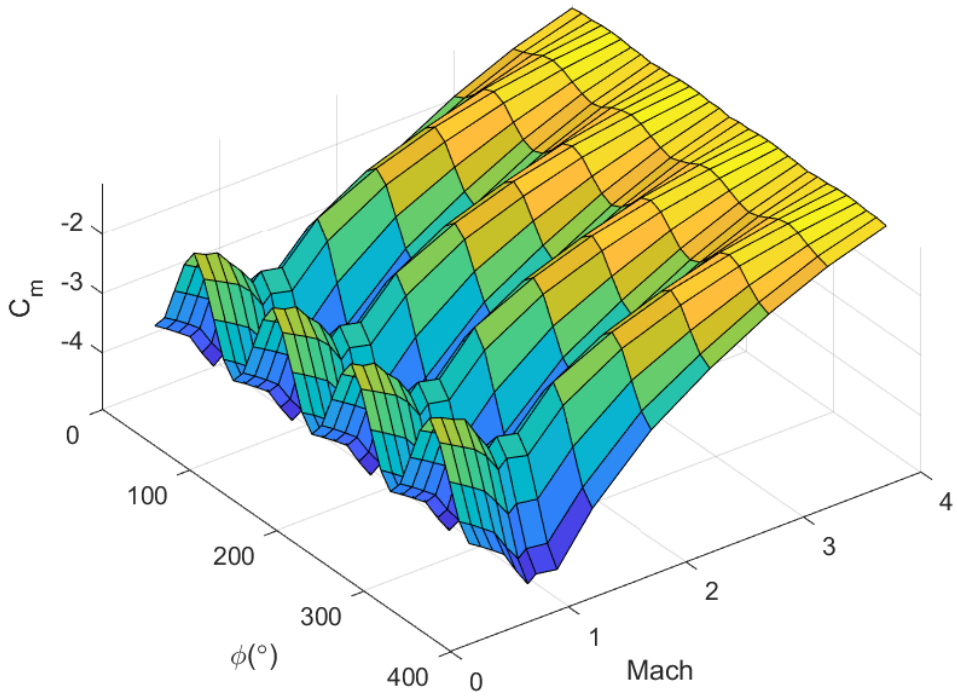

Fig. 21 C_m vs. ϕ and M_∞ for δ = 0° and α_T = 16°

In Figs. 18–21, we can see how the coefficients have a sinusoidal dependence with roll orientation and generally decrease in magnitude with increasing M_∞ in the supersonic regime. As an interesting observation, there seems to be a coupled interaction between ϕ and M_∞ where the sinusoidal dependence on ϕ is decreasing as M_∞ increases. Similar to comparing two roll orientations, we calculate x_{cp} using C_N and C_m for both total angles of attack. The surface plot for $x_{cp}^{\alpha_T=6^\circ}$ versus ϕ and M_∞ at $\alpha_T = 6°$ is shown in Fig. 22 and the surface plot for $x_{cp}^{\alpha_T=16^\circ}$ versus ϕ and M_∞ at $\alpha_T = 16°$ is shown in Fig. 23.

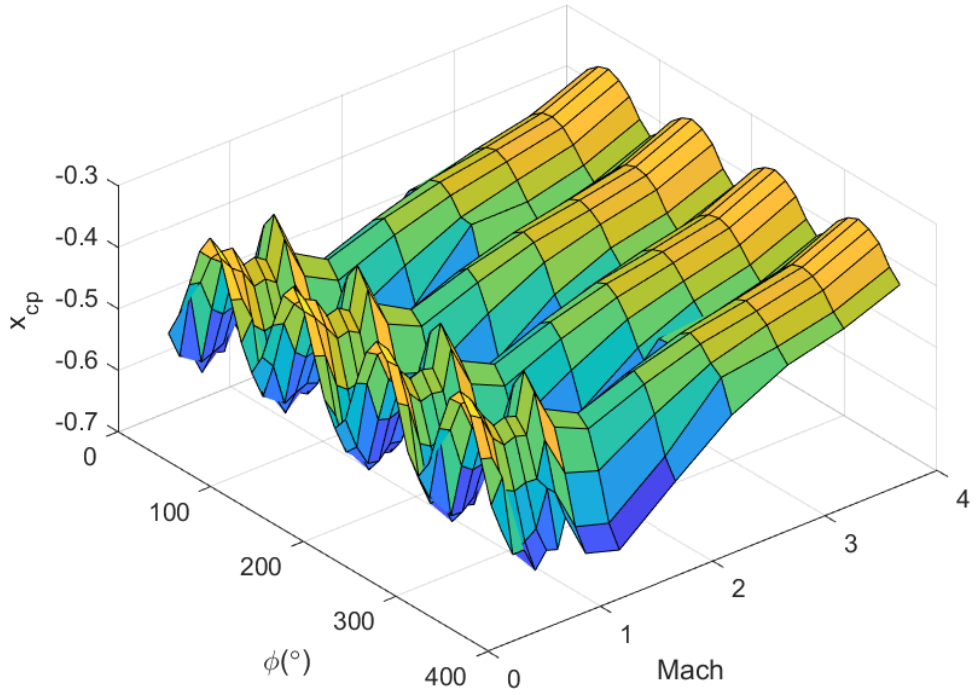

Fig. 22 $x_{cp}^{\alpha_T=6^\circ}$ **vs.** ϕ **and** M_∞ **for δ = 0°**

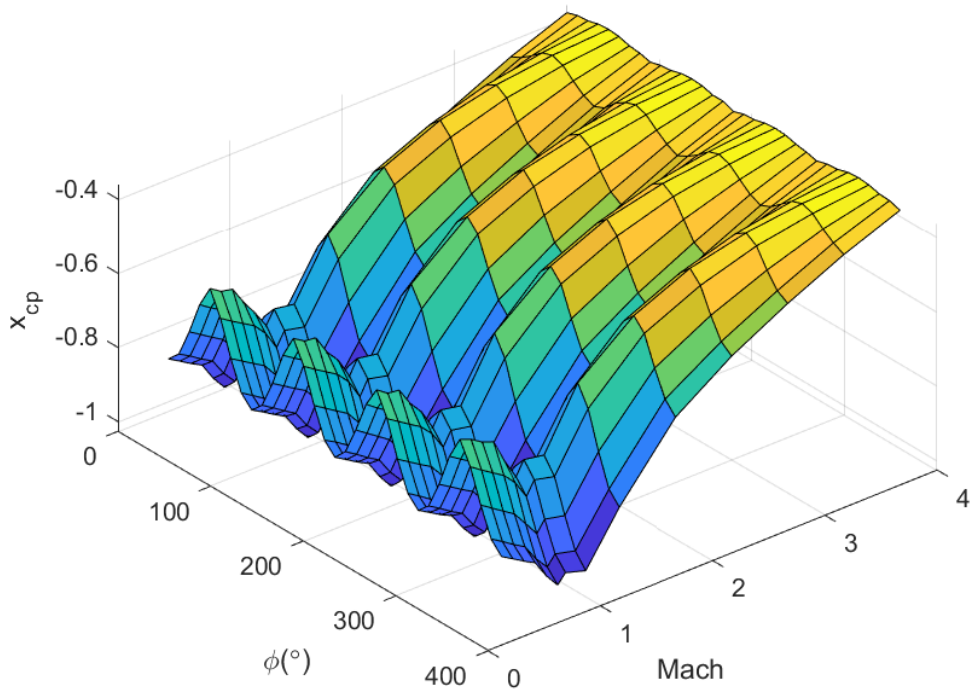

Fig. 23 $x_{cp}^{\alpha_T=16^\circ}$ **vs.** ϕ **and** M_∞ **for δ = 0°**

Once again, we can better understand the comparison to these two surface plots (Figs. 22 and 23) by visualizing $\Delta x_{cp}^{\alpha_T}$ directly, which is shown in Fig. 24. The description of this metric is shown in Eq. 11.

$$\Delta x_{cp}^{\alpha_T} = x_{cp}^{\alpha_T=6^\circ} - x_{cp}^{\alpha_T=16^\circ} \tag{11}$$

Equation 11 means that negative $\Delta x_{cp}^{\alpha_T}$ values indicate a loss in stability while positive $\Delta x_{cp}^{\alpha_T}$ values indicate a gain in stability at $\alpha_T = 16°$. From Fig. 24 it is clear that at the higher total angle of attack, the projectile is more statically stable at the higher incidence angle below approximately $M_\infty = 2.25$. Above $M_\infty = 2.25$, the projectile actually becomes slightly less stable at $\alpha_T = 16°$ compared to $\alpha_T = 6°$.

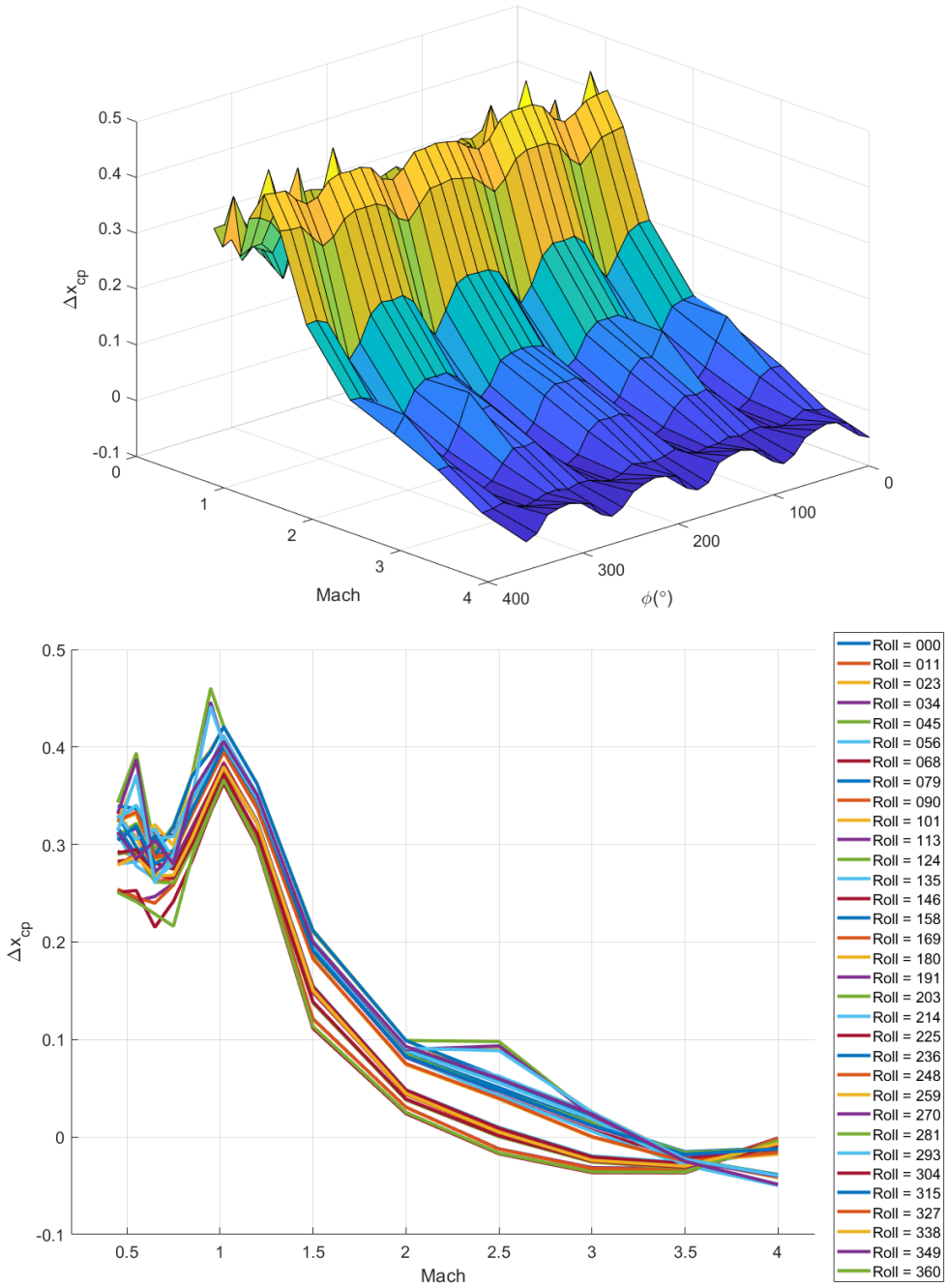

Fig. 24 $\Delta x_{cp}^{\alpha_T}$ between $\alpha_T = 6°$ and $\alpha_T = 16°$ vs. ϕ and M_∞ for $\delta = 0°$ (top) and $\Delta x_{cp}^{\alpha_T}$ between $\alpha_T = 6°$ and $\alpha_T = 16°$ vs. M_∞ for $\delta = 0°$ (bottom) calculated from Eq. 11

The general inference we can make is that the projectile is appropriately designed in the sense that slight changes in total angle of attack either from changes in atmosphere or from aerodynamic maneuvering will lead to instability. Before we can finish documenting the characteristics of this aerodynamic database, the surface plots of C_N and C_m at $\alpha_T = 6°$ and $\alpha_T = 16°$ for additional flap deflection angles are presented in Figs. 25 and 26.

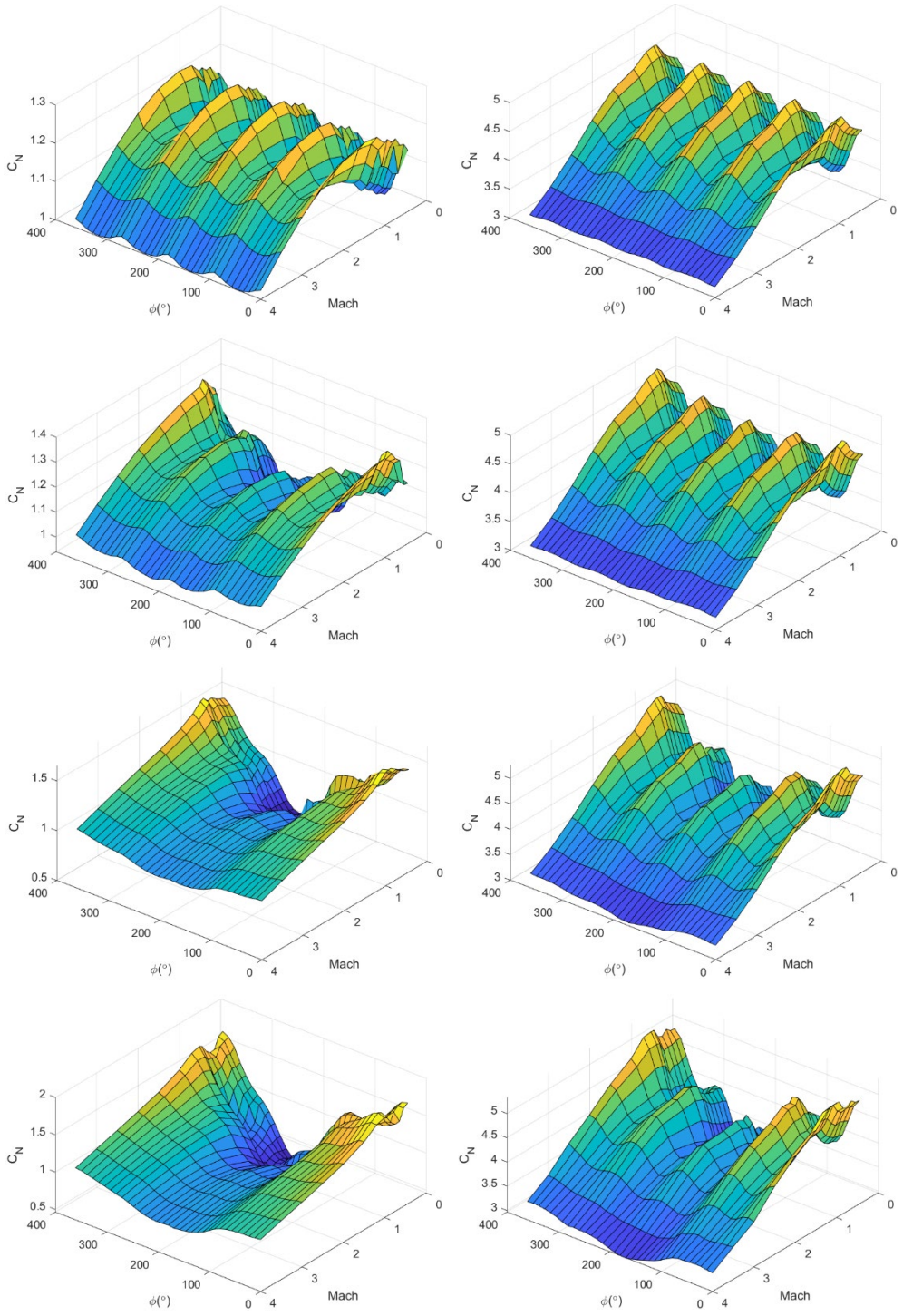

Fig. 25 C_N **vs.** ϕ **and** M_∞ **at** α_T **= 6° (left) and** α_T **= 16° (right) for δ = 0° (first row), δ = 5° (second row), δ = 15° (third row), and δ = 25° (fourth row)**

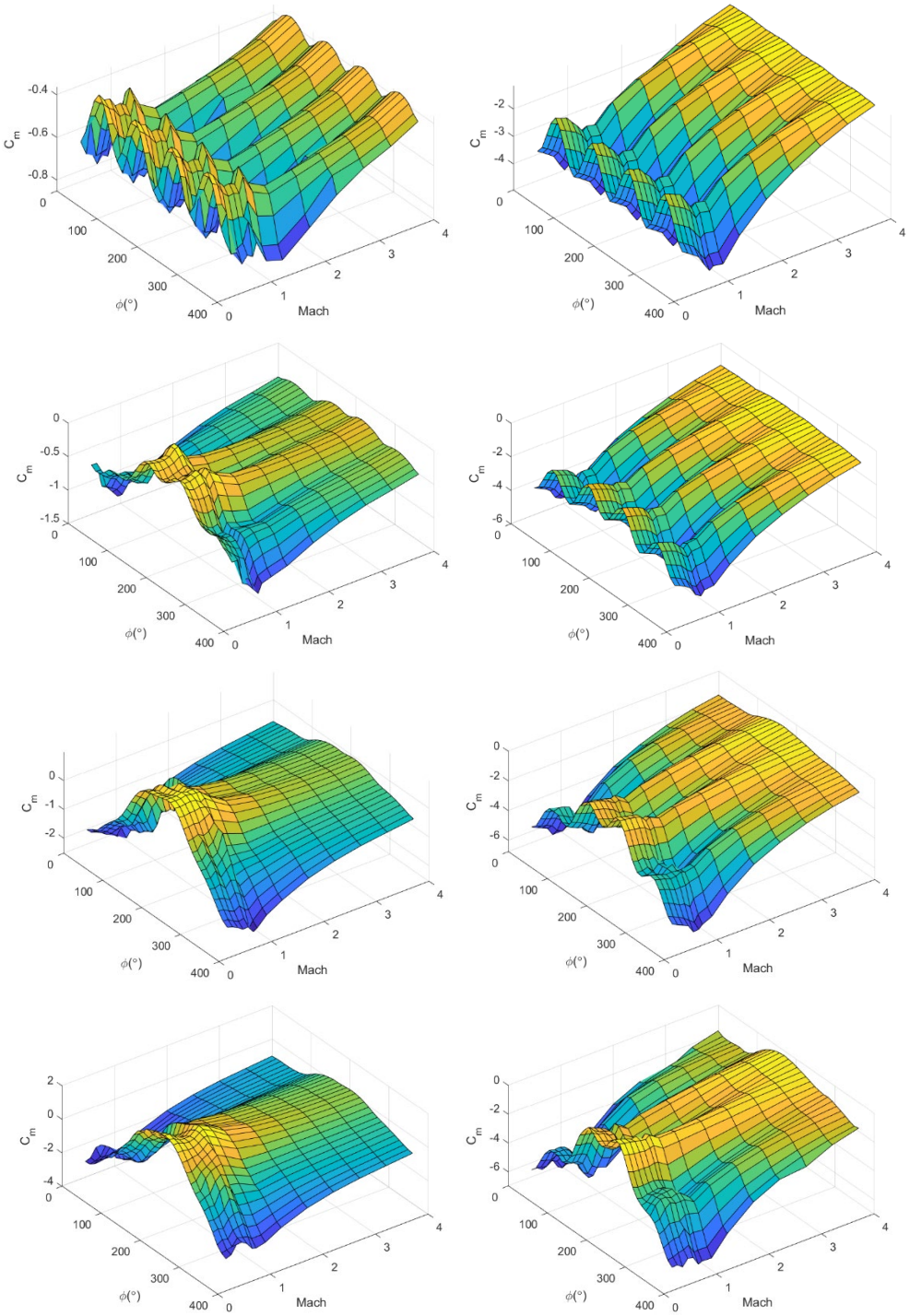

Fig. 26 C_m **vs.** ϕ **and** M_∞ **at** α_T **= 6° (left) and** α_T **= 16° (right) for δ = 0° (first row), δ = 5° (second row), δ = 15° (third row), and δ = 25° (fourth row)**

Again we see strong dependence of both C_N and C_m on roll angle at lower M_∞ in Figs. 25 and 26 just as we observed in Figs. 18–21. What is most interesting is the change in C_N and C_m at α_T = 6° as flap deflection angle increases. For C_N, we observe a simultaneous decrease in oscillating roll-dependent aerodynamics with a

decrease in magnitude near $\phi = 180°$ (flying upside down) and an increase in value near $\phi = 0°$ (flying right-side up). For C_m, we observe a simultaneous decrease in oscillating roll dependent aerodynamics with an increase in value near $\phi = 180°$ and a decrease in value near $\phi = 0°$. While these changes are also present at the higher angle of attack, $\alpha_T = 16°$, they are less dramatic.

Figure 4 shows how positive flap deflection for fin 1 (δ_1) corresponds to an increase in the local angle of attack of the flap relative to the wind vector when the projectile is flying right-side up. The opposite is also true where positive flap deflection corresponds to a decrease in local angle of attack of the flap relative to the wind vector when the projectile is flying upside down. At low total angles of attack, the aerodynamics of the flap might have a more dramatic effect on the aerodynamics of the projectile since the flap is not in the shadow of the fin. Conversely, at higher angles of attack, the aerodynamics dependent on the rigid surfaces of the projectile (not the deflecting flap) have greater influence over the entire projectile's aerodynamics and thus decrease the relative impact of the local aerodynamics of the deflected flap.

4.3 Analyzing C_l, C_A, C_S, and C_n

We can finish documenting the aerodynamic database for the projectile by evaluating the remaining aerodynamic coefficients, which are rolling moment coefficient, C_l, axial force coefficient, C_A, side force coefficient, C_S, and yawing moment coefficient, C_n. Similar to how we analyzed the results for C_N and C_m across M_∞, total angle of attack, and roll angle in Figs. 9–26, we will look at C_l, C_A, C_A, C_S, and C_n in Figs. 27–34.

The first figure in this series, Fig. 27, shows both $\alpha_T = 6°$ and $\alpha_T = 16°$ for C_l versus roll angle and Mach number. At $\delta = 0°$, the surface plots for each α_T exhibit similar behavior with a slight increase in magnitude at the higher α_T. The behavior is roll reversal where the sinusoidal C_l dependence on roll angle shifts in phase from what was previously a peak in C_l to what is now a trough as M_∞ increases. The roll reversal phenomenon is likely due to how the pressure distribution across the fins changes as the shocks over the control surfaces increase in strength and the effect of vortices emanating from the fins.[10,12] However, as we analyze the other surface plots across increasing flap deflection (third and fourth rows) in Fig. 27, we see that the roll reversal phenomenon diminishes substantially at the lower total incidence angle, $\alpha_T = 6°$. Yet, even though the roll reversal phenomenon is diminished, there is still a subtle dependence on ϕ. At the higher incidence angle, $\alpha_T = 16°$, we see that the roll dependence and the roll reversal behavior remains but becomes more complex where troughs and peaks are not necessarily uniform in magnitude and the

trends with respect to M_∞ vary with roll angle even at roll angles equally spaced in correspondence with the period of the roll dependence.

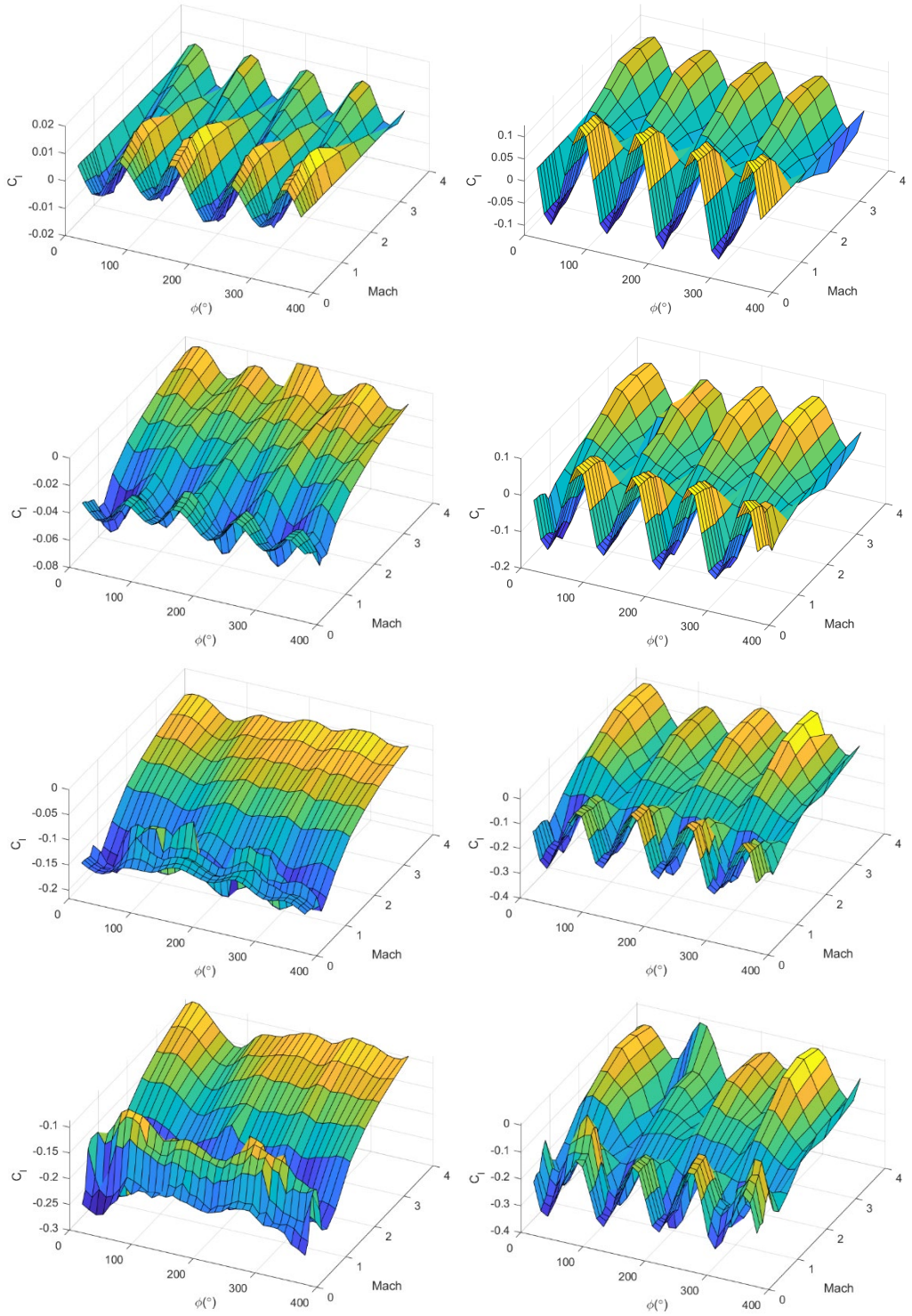

Fig. 27 C_l **vs.** ϕ **and** M_∞ **at** α_T **= 6° (left) and** α_T **= 16° (right) for δ = 0° (first row), δ = 5° (second row), δ = 15° (third row), and δ = 25° (fourth row)**

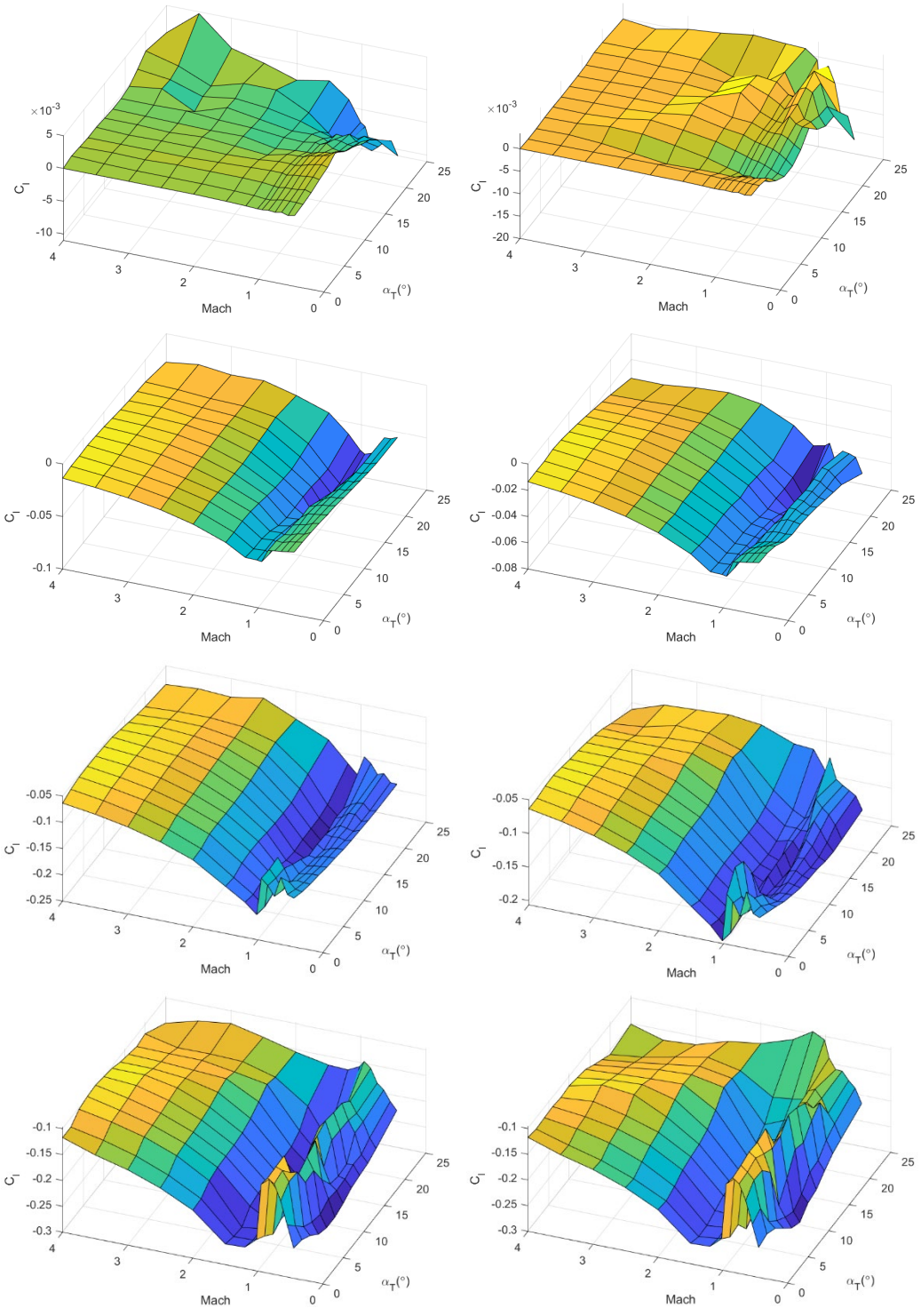

Fig. 28 C_l **vs.** α_T **and** M_∞ **at** $\phi = 0°$ **(left) and** $\phi = 45°$ **(right) for** $\delta = 0°$ **(first row),** $\delta = 5°$ **(second row),** $\delta = 15°$ **(third row), and** $\delta = 25°$ **(fourth row)**

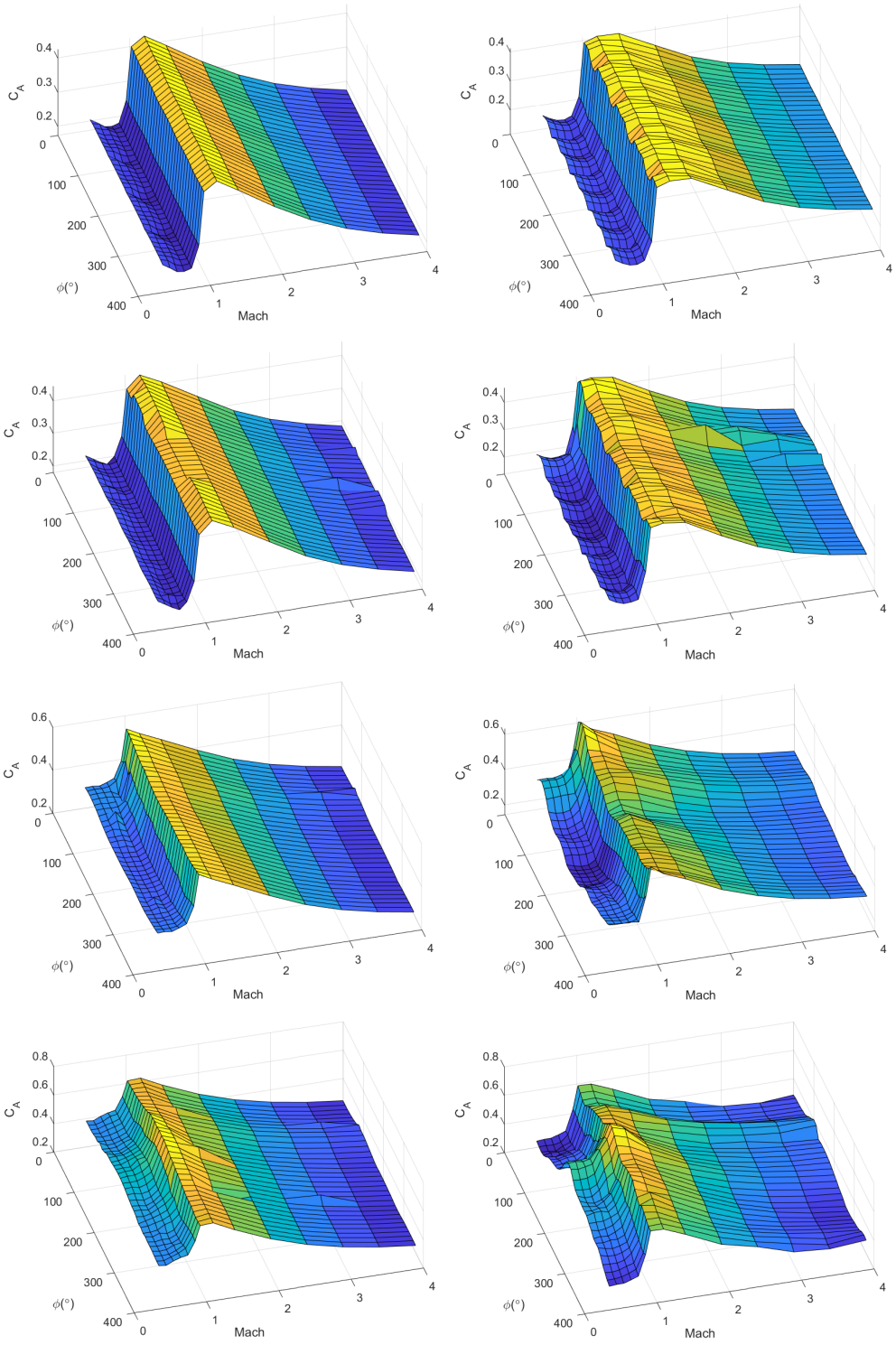

Fig. 29 C_A **vs.** ϕ **and** M_∞ **at** α_T **= 6° (left) and** α_T **= 16° (right) for δ = 0° (first row), δ = 5° (second row), δ = 15° (third row), and δ = 25° (fourth row)**

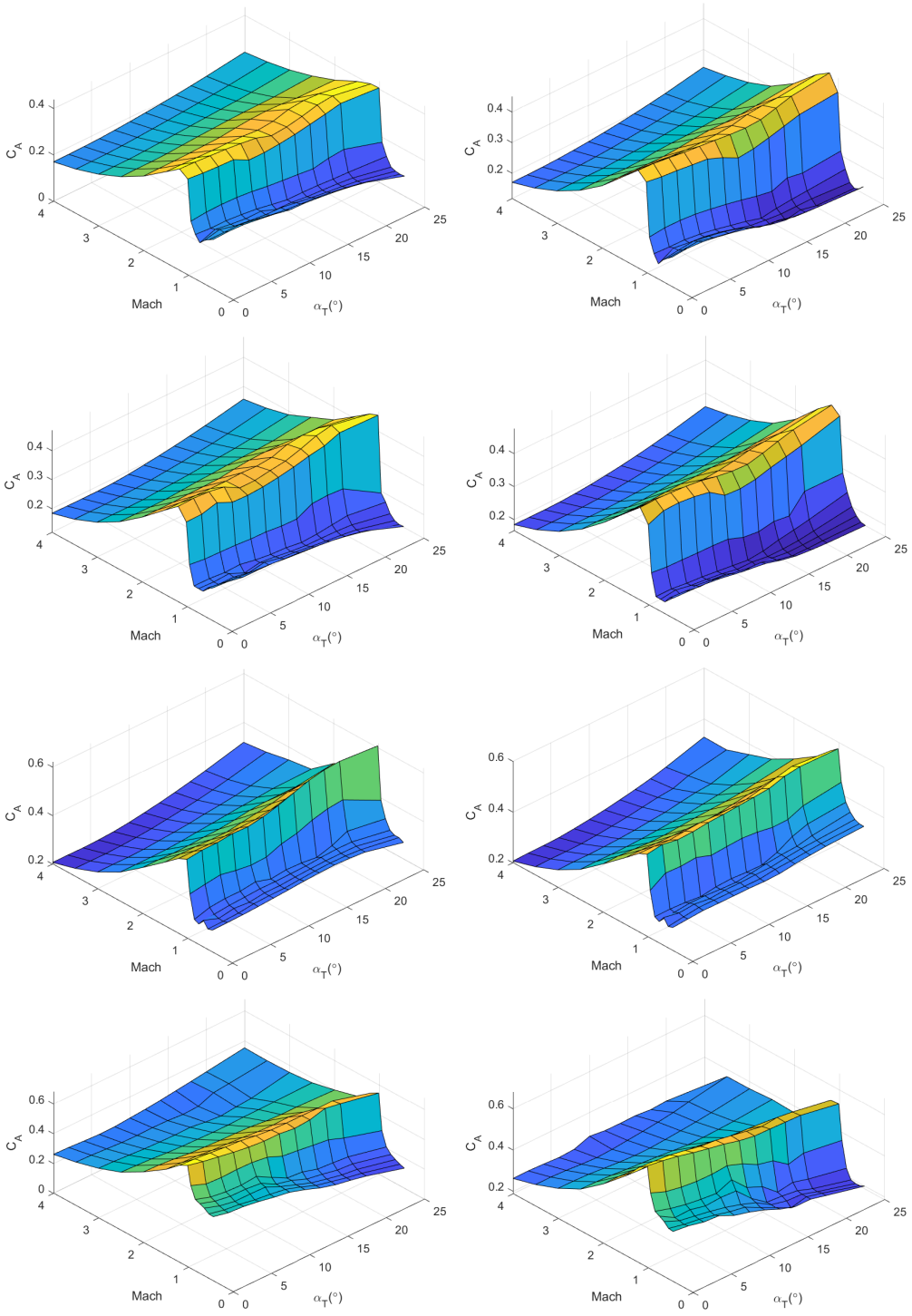

Fig. 30 C_A **vs.** α_T **and** M_∞ **at** ϕ **= 0° (left) and** ϕ **= 45° (right) for δ = 0° (first row), δ = 5° (second row), δ = 15° (third row), and δ = 25° (fourth row)**

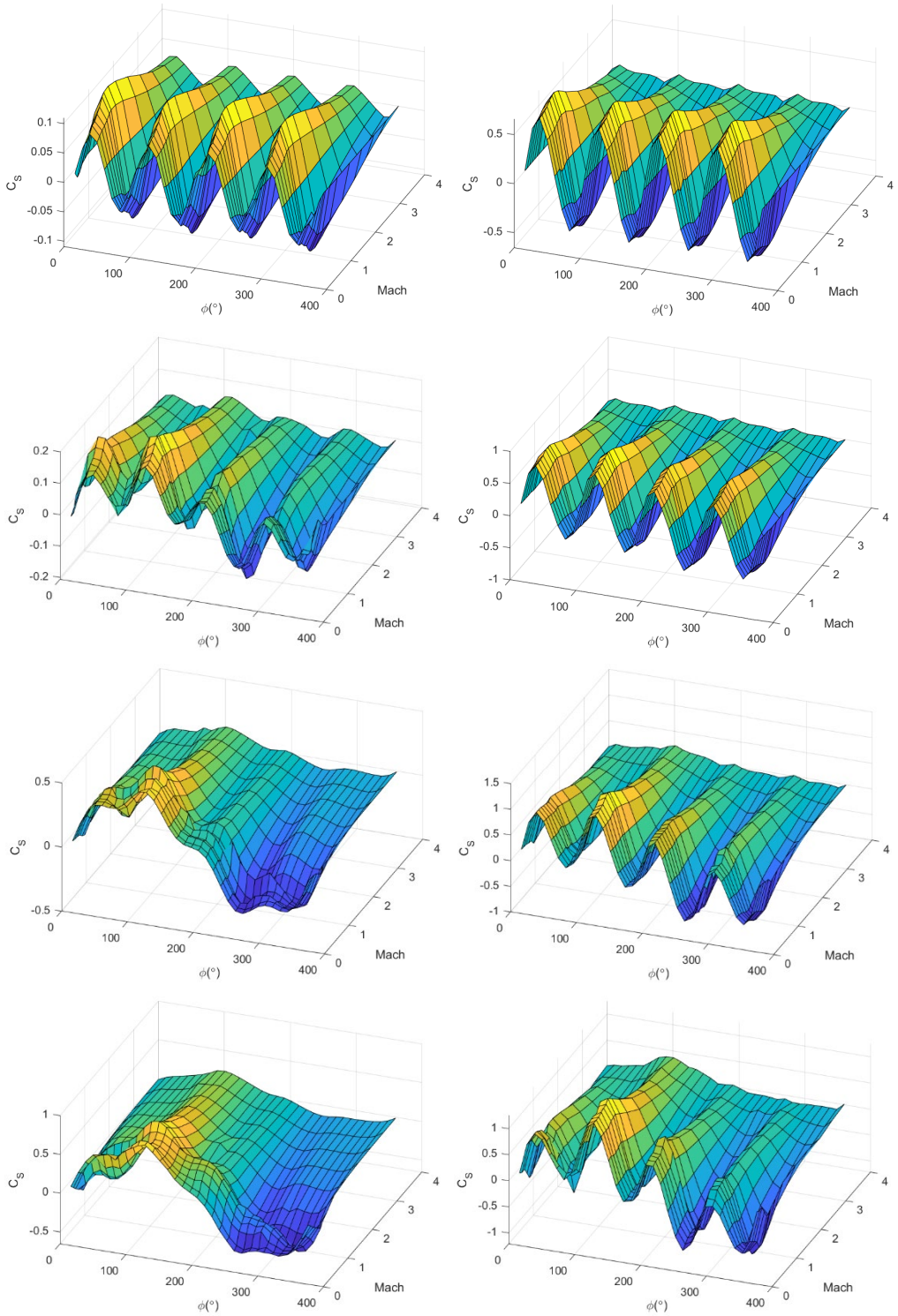

Fig. 31 C_S **vs.** ϕ **and** M_∞ **at** α_T **= 6° (left) and** α_T **= 16° (right) for δ = 0° (first row), δ = 5° (second row), δ = 15° (third row), and δ = 25° (fourth row)**

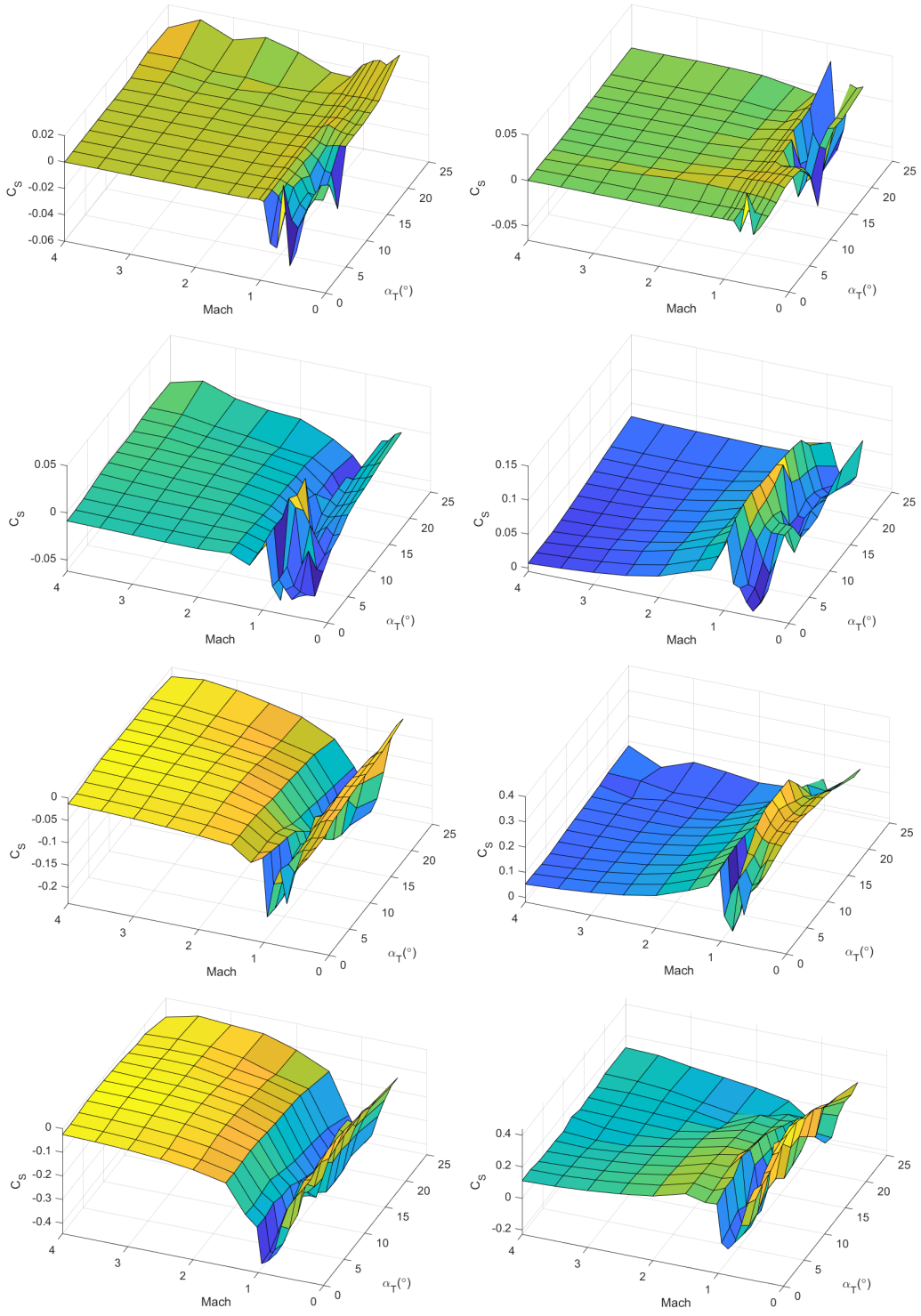

Fig. 32 C_S **vs.** α_T **and** M_∞ **at** ϕ **= 0° (left) and** ϕ **= 45° (right) for δ = 0° (first row), δ = 5° (second row), δ = 15° (third row), and δ = 25° (fourth row)**

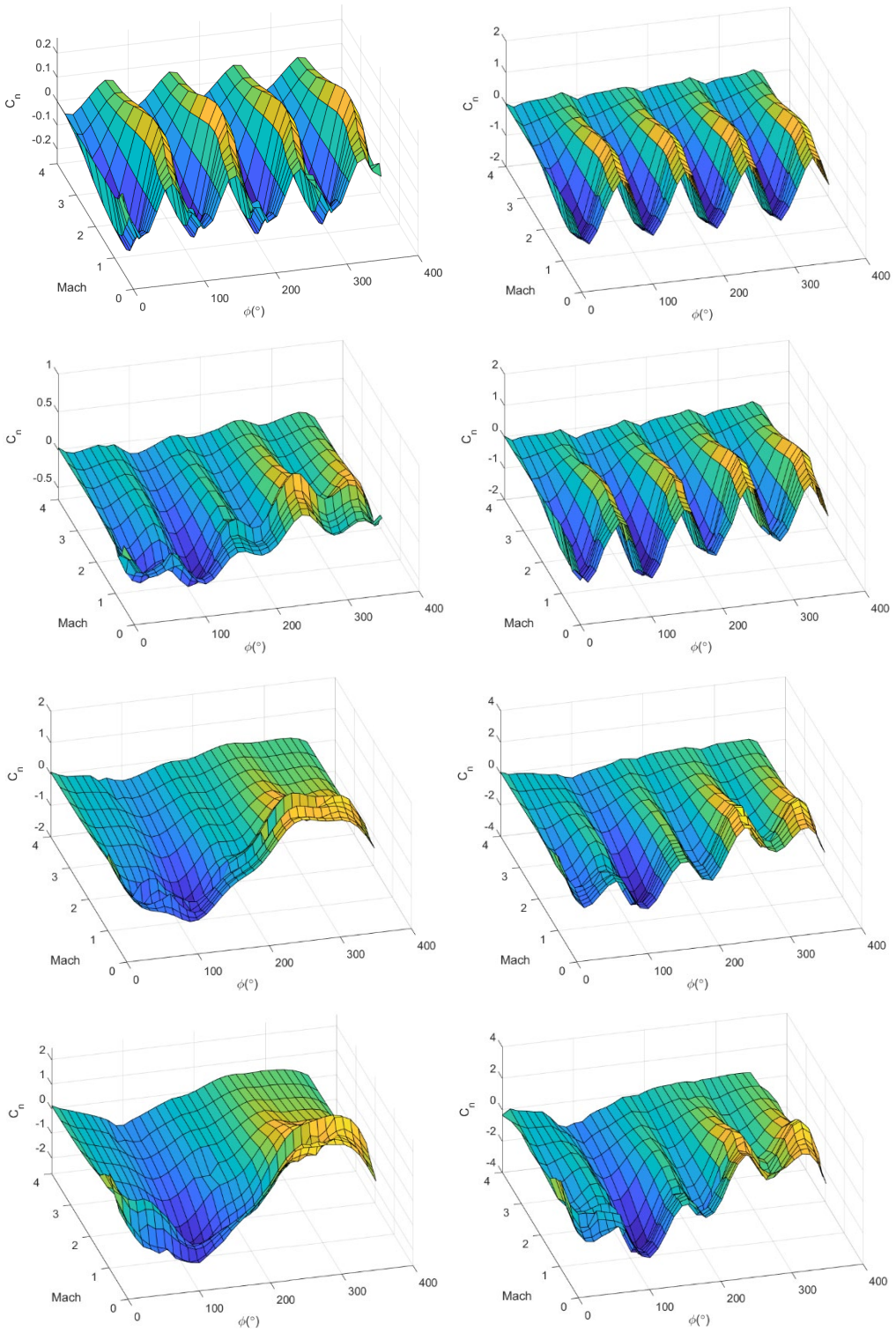

Fig. 33 C_n **vs.** ϕ **and** M_∞ **at** α_T **= 6° (left) and** α_T **= 16° (right) for δ = 0° (first row), δ = 5° (second row), δ = 15° (third row), and δ = 25° (fourth row)**

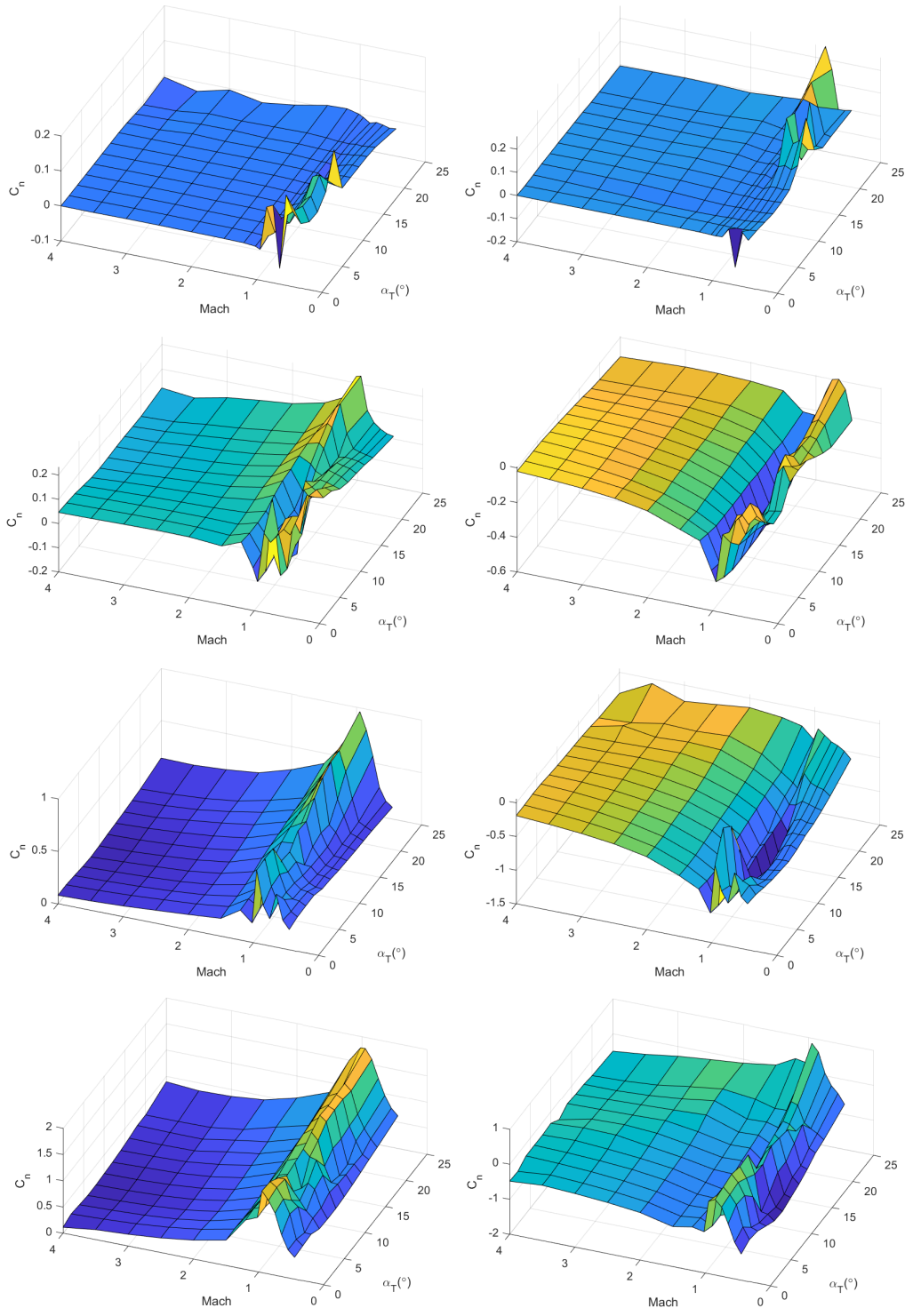

Fig. 34 C_n **vs.** α_T **and** M_∞ **at** ϕ **= 0° (left) and** ϕ **= 45° (right) for δ = 0° (first row), δ = 5° (second row), δ = 15° (third row), and δ = 25° (fourth row)**

The roll reversal phenomenon as seen in Fig. 27 is also evident in Fig. 35, which shows a comparison of C_l with respect to ϕ at M_∞ between 1.02 and 4.00 for δ = 0°, and α_T = 6°. Figure 35 clearly illustrates the roll reversal phenomenon previously mentioned as the peaks in the roll dependence become troughs and vice versa with increasing M_∞.

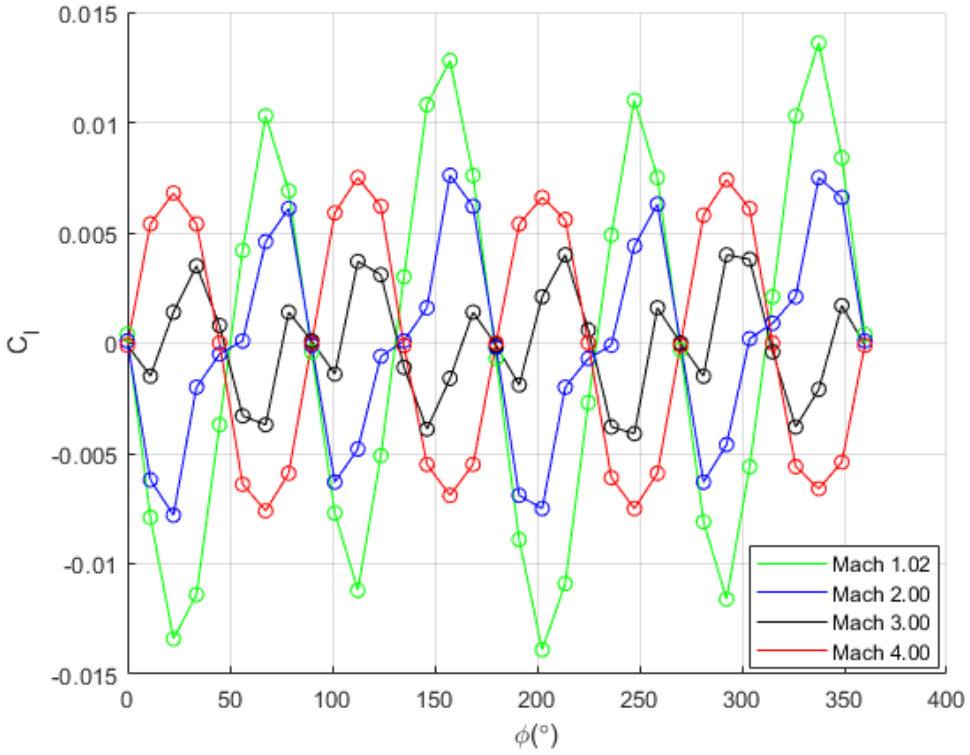

Fig. 35 Roll reversal phenomenon demonstrated by comparing C_l vs. ϕ at M_∞ = 1.02 (green), M_∞ = 2.00 (blue), M_∞ = 3.00 (black), and M_∞ = 4.00 (red) for δ = 0° and α_T = 6°

The figures generally show the decrease in magnitude of all aerodynamic coefficients with increasing M_∞ in the supersonic region, which is an expected result. Additionally, it should be remembered that this inviscid aerodynamic database will only generate the inviscid, or pressure dominated, component of the coefficients. The aerodynamic coefficient C_A is most impacted since the viscous, skin friction component is not included.

Figures 31 and 33 illustrate how C_S and C_n have strong roll dependence at lower M_∞ and lower flap deflection angles, which is similar to C_l. As M_∞ increases, the aerodynamic coefficient magnitudes decrease. As flap deflection angle increases, the roll dependence does not decrease but it does change in shape, and it changes most dramatically at the lower total angle of attack α_T = 6°, which is similar to C_l.

4.4 Comparison to High-Fidelity CFD and Wind Tunnel Experiment

This inviscid aerodynamic database is now compared to higher fidelity Reynolds Averaged Navier-Stokes (RANS) simulations using the CFD^{++} solver[6] and wind tunnel experiments that were conducted on a subscale model at Florida State University.[8,9] These comparisons are presented in Figs. 36–41. In all of the figures, flowCart data is plotted in black, RANS data is plotted in green, and wind tunnel data is plotted in red.

In general, all three methods compare well with some differences increasing at the higher Mach numbers. The largest discrepancy is in the prediction of C_A, which is expected for flowCart, since it does not include the viscous component. In the wind tunnel data, while the presence of the sting is accounted for by measuring the base pressure, this correction is always subject to some inaccuracy. The most accurate axial force, or drag, is usually obtained via free-flight or aeroballistic testing. Until that data is available, it is best to assume the axial force is in the range bounded by the wind tunnel data and the high-fidelity (CFD^{++}) predictions.

The RANS CFD prediction are, in general, in better agreement with the wind tunnel data than the flowCart data. The largest difference between flowCart predictions and the CFD was for C_m at the lower incidence angle, Fig. 37. The better prediction of the roll up of the vortical structures on the fins by the RANS CFD is believed primarily responsible for these differences.[6] However, the comparison of the flowCart and RANS CFD is still quite good. Difference between the RANS CFD and the wind tunnel data can be due to inaccurate prediction of the center of pressure (e.g., inaccurate leeside separation or vortex formation prediction) or possible off calibration of the sting bending leading to inaccurate incidence angle estimates. These differences are taken into account in aerodynamic model generation via weighting each data source.[2]

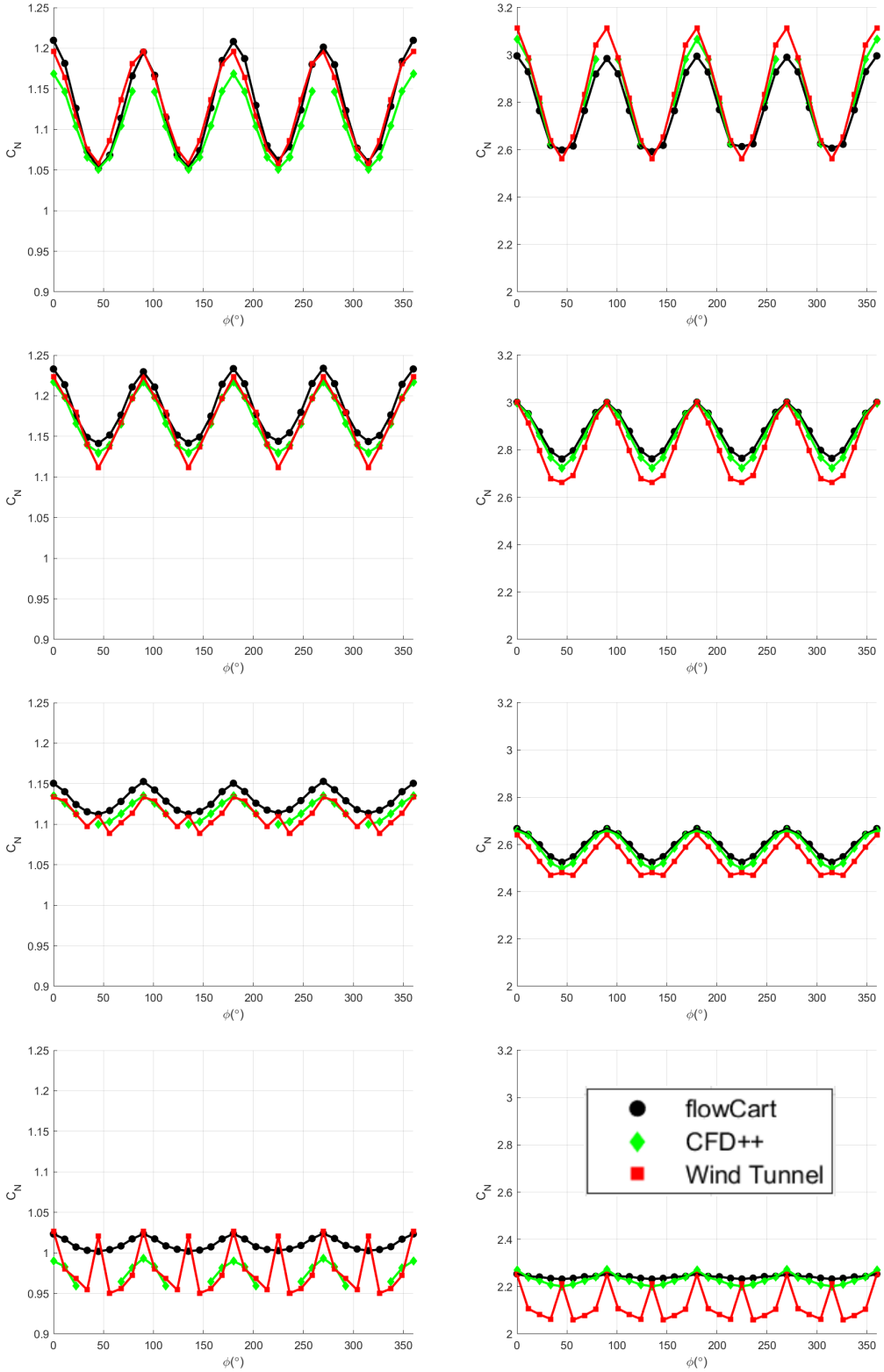

Fig. 36 Comparisons of C_N vs. ϕ for $M_\infty = 0.75$ (first row), $M_\infty = 2.00$ (second row), $M_\infty = 3.00$ (third row), and $M_\infty = 4.00$ (fourth row), at $\alpha_T = 6°$ (left), $\alpha_T = 12°$ (right) for $\delta = 0°$

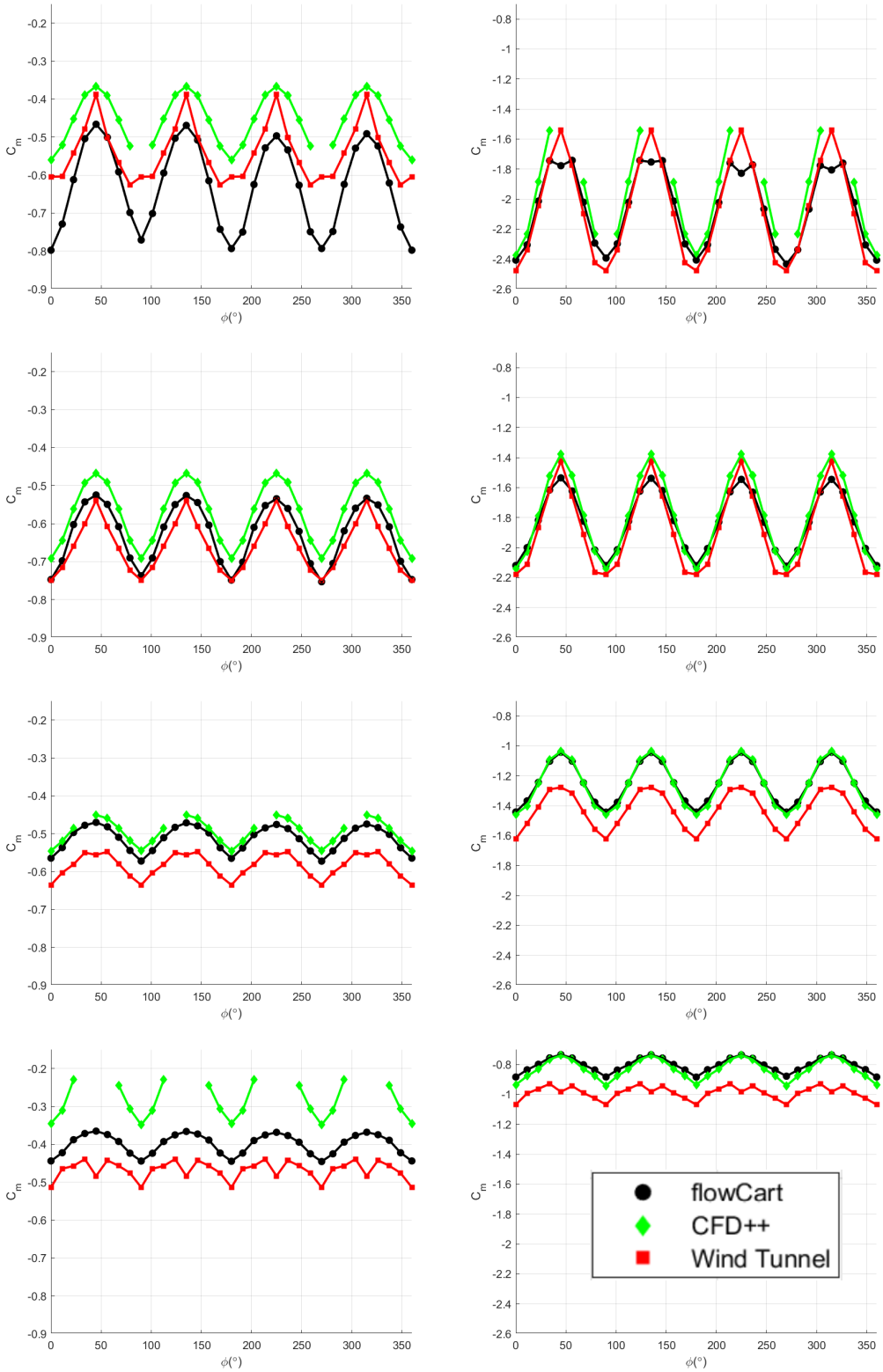

Fig. 37 Comparisons of C_m vs. ϕ for $M_\infty = 0.75$ (first row), $M_\infty = 2.00$ (second row), $M_\infty = 3.00$ (third row), and $M_\infty = 4.00$ (fourth row), at $\alpha_T = 6°$ (left), $\alpha_T = 12°$ (right) for $\delta = 0°$

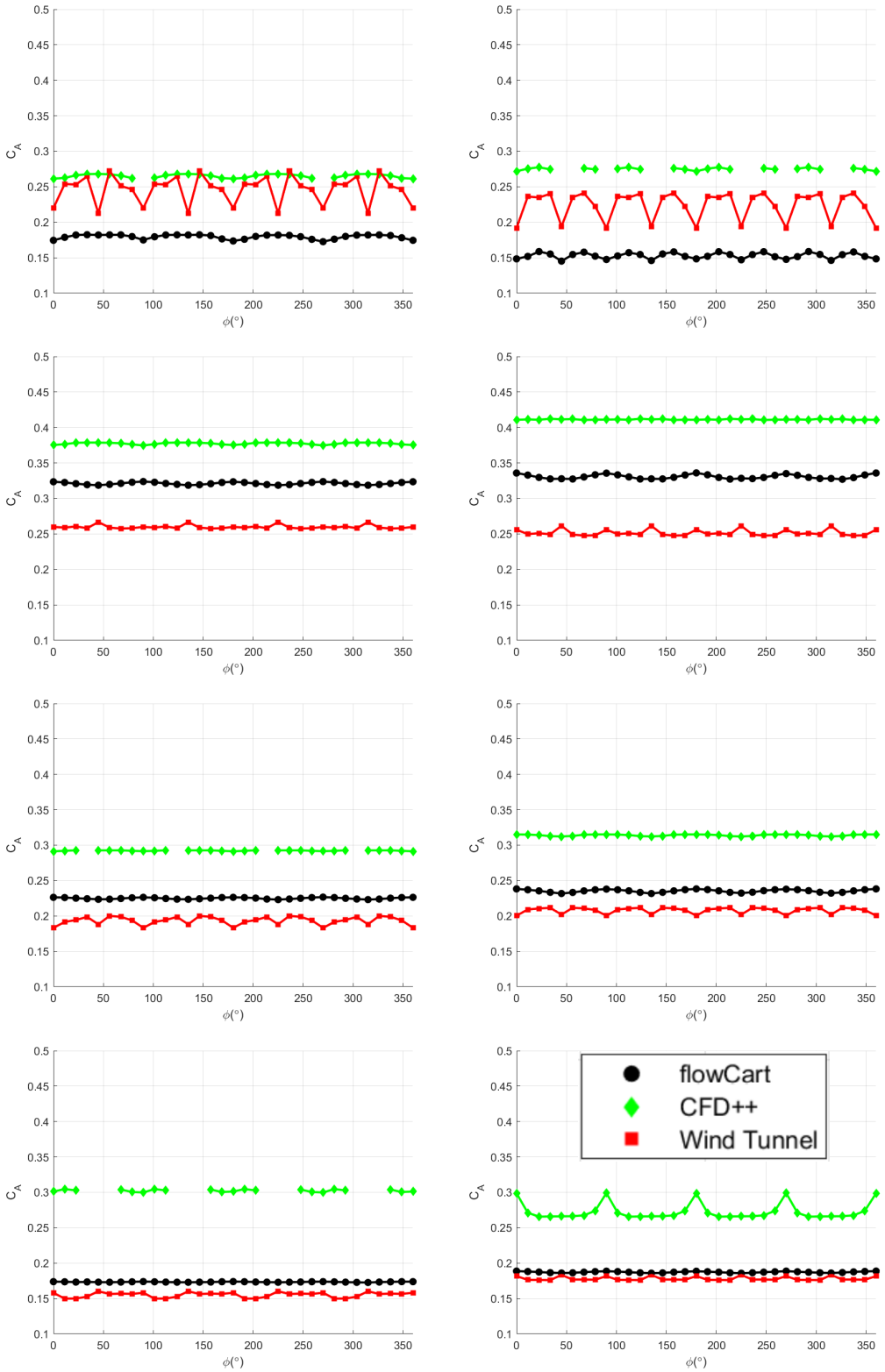

Fig. 38 Comparisons of C_A vs. ϕ for $M_\infty = 0.75$ (first row), $M_\infty = 2.00$ (second row), $M_\infty = 3.00$ (third row), and $M_\infty = 4.00$ (fourth row), at $\alpha_T = 6°$ (left), $\alpha_T = 12°$ (right) for $\delta = 0°$

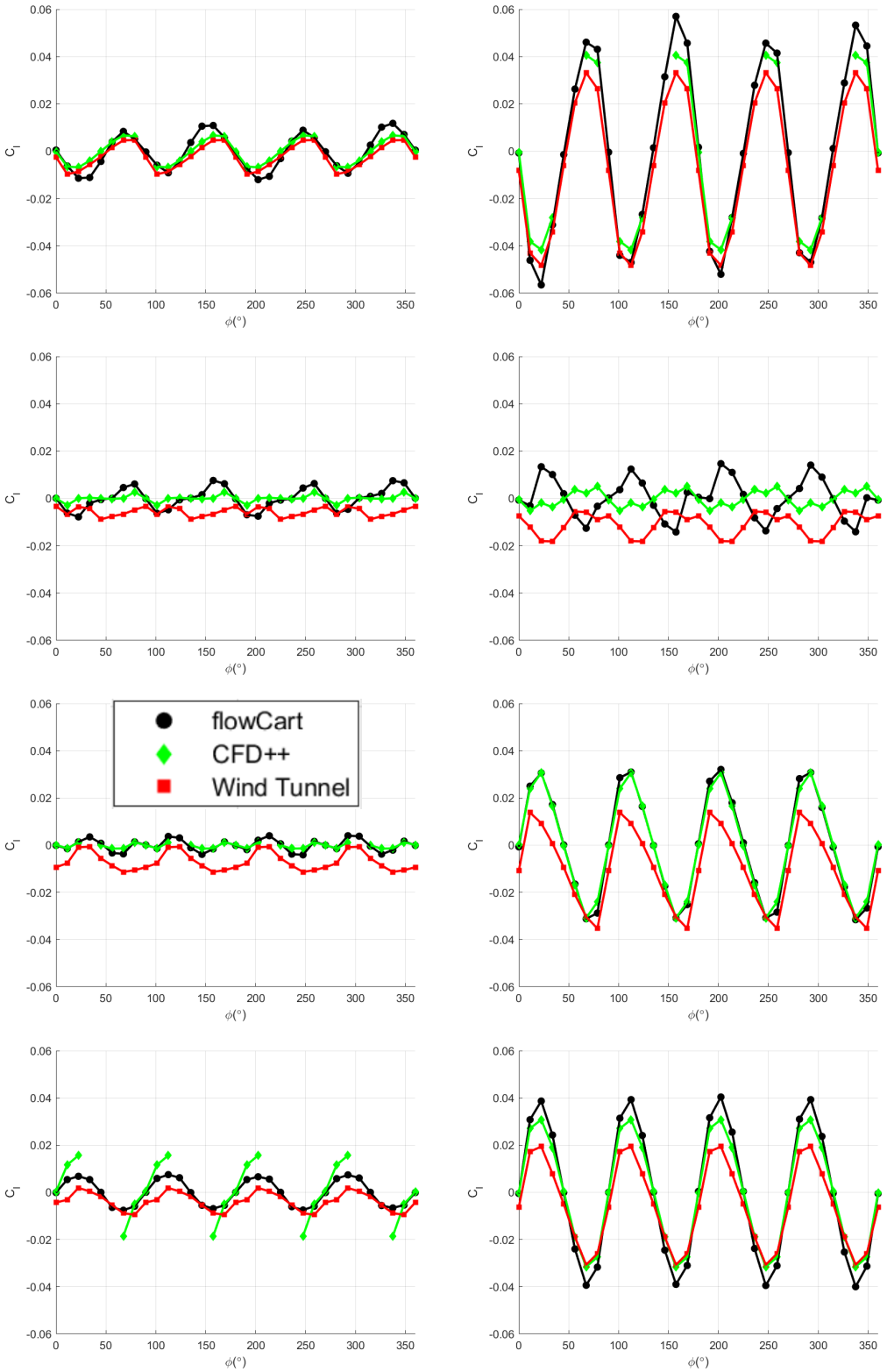

Fig. 39 Comparisons of C_l vs. ϕ for $M_\infty = 0.75$ (first row), $M_\infty = 2.00$ (second row), $M_\infty = 3.00$ (third row), and $M_\infty = 4.00$ (fourth row), at $\alpha_T = 6°$ (left), $\alpha_T = 12°$ (right) for $\delta = 0°$

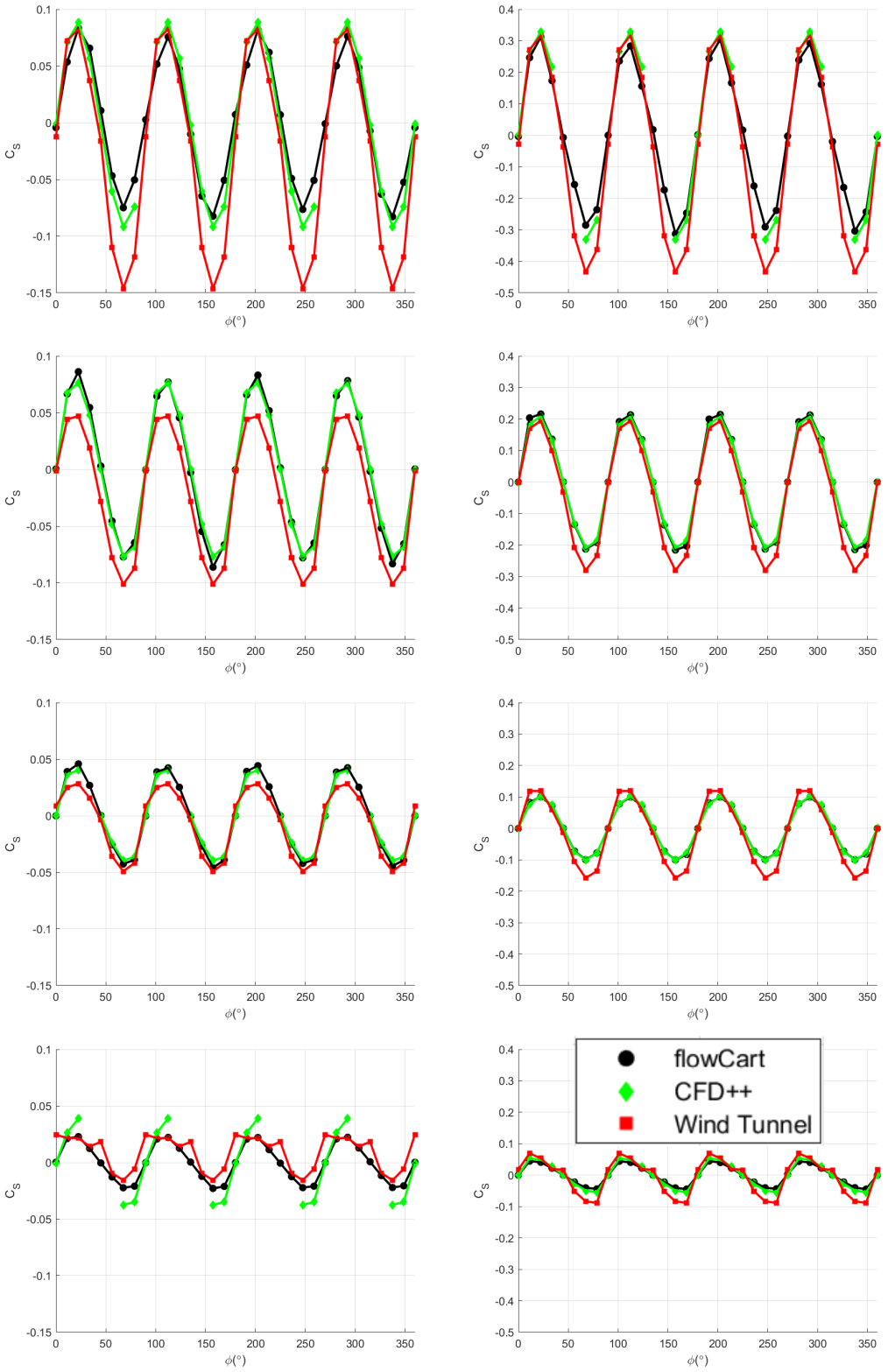

Fig. 40 Comparisons of C_S vs. ϕ for $M_\infty = 0.75$ (first row), $M_\infty = 2.00$ (second row), $M_\infty = 3.00$ (third row), and $M_\infty = 4.00$ (fourth row), at $\alpha_T = 6°$ (left), $\alpha_T = 12°$ (right) for $\delta = 0°$

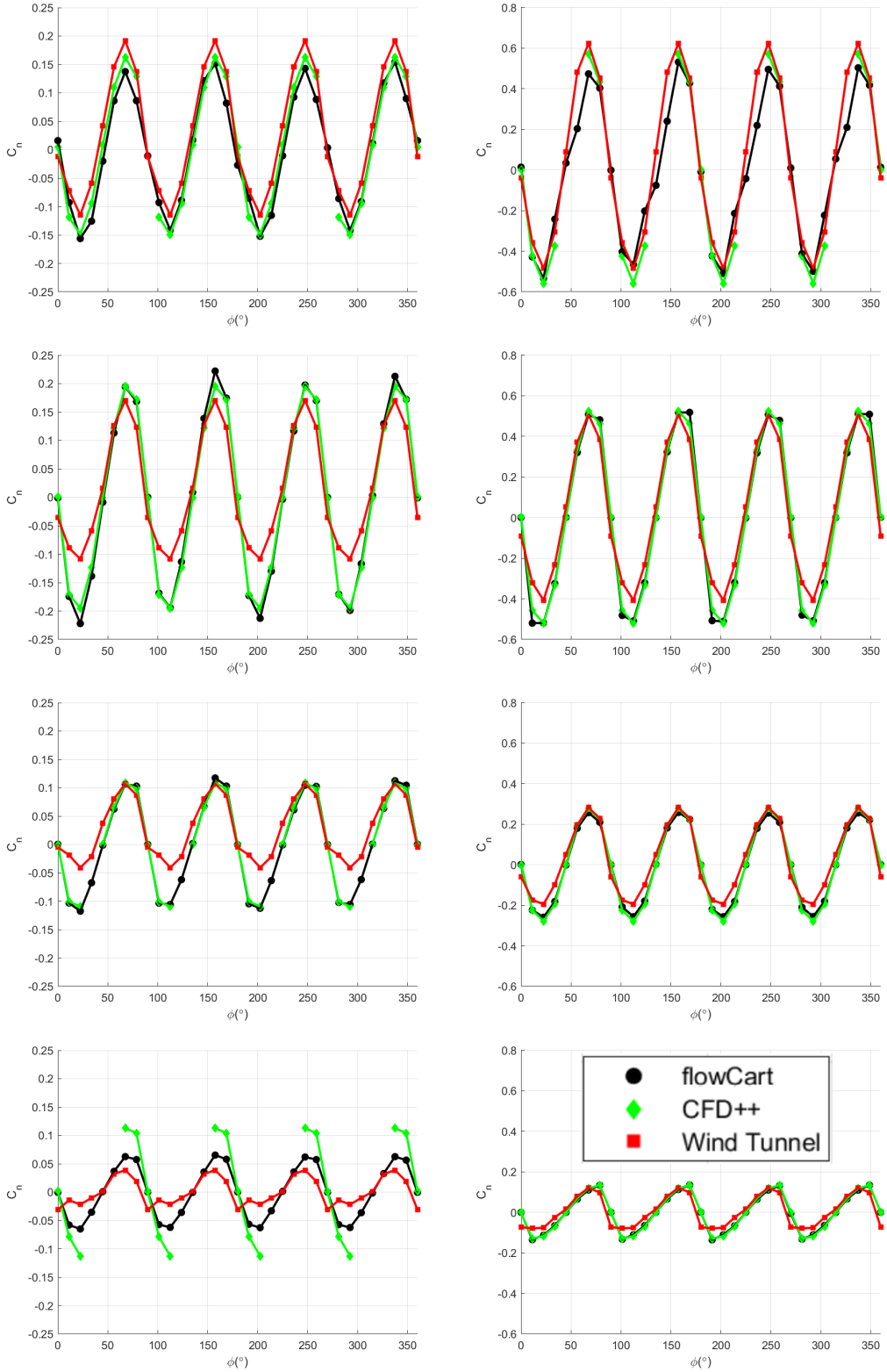

Fig. 41 Comparisons of C_n vs. ϕ for $M_\infty = 0.75$ (first row), $M_\infty = 2.00$ (second row), $M_\infty = 3.00$ (third row), and $M_\infty = 4.00$ (fourth row), at $\alpha_T = 6°$ (left), $\alpha_T = 12°$ (right) for $\delta = 0°$

5. Conclusion

The characteristics of an inviscid aerodynamic database for a high-speed guided projectile was documented using surface plots. On average, over 99% of the data in this inviscid aerodynamic database is raw data but some data was interpolated using polynomial and Fourier regression techniques. The broad conclusions drawn from analyzing the topology of the inviscid aerodynamic database are as follows:

- Aerodynamic coefficients generally decrease in magnitude with increasing M_∞ in the supersonic regime above $M_\infty = 1.2$ as expected.
- C_N and C_m increases in magnitude with increasing α_T as expected.
- The "x" roll orientation ($\phi = 45°$) is generally less statically stable than the "+" roll orientation ($\phi = 0°$).
- Sinusoidal dependence of aerodynamic coefficients on ϕ decreases as M_∞ increases and as flap deflection, δ, increases.
- The vehicle is appropriately designed to preserve static stability during flight with respect to total angle of attack.
- Sinusoidal roll reversal phenomenon in C_l was observed with increasing M_∞.
- flowCart predicts C_m less accurately in cases where the viscous roll up of the vortical structures is an important aspect of approximating the pressure distribution over the projectile.
- flowCart generally shows good agreement with RANS CFD and wind tunnel data.

6. References

1. Paul JL, Vasile JD, DeSpirito J. Comparison of aeroprediction methods for guided munitions. DEVCOM Army Research Laboratory (US); 2021 Sep. Report No.: ARL-TR-9287.

2. Burchett BT, Paul JL, Vasile JD, Bryson JT. A high-fidelity, roll-dependent aerodynamic model for a long-range, high-speed missile. DEVCOM Army Research Laboratory (US); 2021 July. Report No.: ARL-TR-9236.

3. Vasile JD, Bryson JT, Gruenwald BC, Fairfax LD, Strohm LS, Fresconi FE. A multi-disciplinary approach to design long range guided projectiles. 2020 AIAA Science and Technology Forum. Paper No.: AIAA-2020-1993; 2020 Jan.

4. Vasile JD, Bryson JT, Fresconi FE. Aerodynamic design optimization of long-range projectiles using missile DATCOM. 2020 AIAA Science and Technology Forum. Paper No.: AIAA-2020-1762; 2020 Jan.

5. Bryson JT, Vasile JD, Gruenwald, BC, Sahu, J, Fresconi, F. Modeling and flight dynamics of a projectile with nonlinear, roll-dependent aerodynamics. AIAA SciTech Forum; 2021 Jan 11–15 & 19–21. Virtual Event. doi: 10.2514/6.2021-0823.6.

6. Vasile JD, Sahu J. Roll orientation-dependent aerodynamics of a long-range projectile. DEVCOM Army Research Laboratory (US); 2020 Aug. Report No.: ARL-TR-9017.

7. Vasile JD, Bryson JT, Sahu J, Paul Justin L. Aerodynamic dataset generation of a long-range projectile. DEVCOM Army Research Laboratory (US); 2020 Aug. Report No.: ARL-TR-9019.8.

8. Pokela R, Kumar R, Vasile J. Experimental and computational aerodynamic characterization of a generic high-speed projectile configuration. AIAA Aviation Forum; 2021 Aug. AIAA-2021-2607.

9. Pokela R, Kumar R, Vasile JD, DeSpirito. Aerodynamic characterization of a generic high-speed projectile configuration. Manuscript submitted to AIAA Journal of Spacecraft and Rockets.

10. Bryson J, Vasile J, Gruenwald B, Fresconi F. Control surface design analysis and actuation requirements development for munitions. Proceedings of the AIAA SciTech 2020 Forum; 2020 Jan 6–10. AIAA SciTech 2020–0020.

11. Aftosmis MJ, Berger MJ, Adomavicius G. A parallel multilevel method for adaptively refined Cartesian grids with embedded boundaries. 38th Aerospace Sciences Meeting and Exhibit; 2000. AIAA Paper 2000-0808.

12. Heeg J. Control surface interaction effects of the active aeroelastic wing wind tunnel model. 47th AIAA/ASME/ASCE/AHS/ASC Structures, Structural Dynamics, and Materials Conference. 2006. AIAA Paper 2006-2185.

List of Symbols, Abbreviations, and Acronyms

α	angle of attack
α_T	total angle of attack
β	sideslip angle
C_A	axial force coefficient
C_l	rolling moment coefficient
C_m	pitching moment coefficient
C_N	normal force coefficient
C_n	yawing moment coefficient
C_S	side force coefficient
δ	flap deflection angle
ϕ	roll angle
M_∞	Mach number
ARL	Army Research Laboratory
CFD	computational fluid dynamics
DEVCOM	US Army Combat Capabilities Development Command
NASA	National Aeronautics and Space Administration
RANS	Reynolds-averaged Navier–Stokes

1 (PDF) DEFENSE TECHNICAL INFORMATION CTR DTIC OCA

1 (PDF) DEVCOM ARL FCDD RLB CI TECH LIB

2 (PDF) DEVCOM AC RDAR MEM A M DUCA G RODEBAUGH

1 (PDF) USAFA E STEPHEN

1 (PDF) USAFRL B DICKINSON

1 (PDF) AFOSR G ABATE

8 (PDF) DEVCOM AVMC FCDD AMS MMA L AUMAN P CROSS J DOYLE Z HALL M MCDANIEL C ROSEMA B WILKS J LUSK

1 (PDF) SYSTEMS ENG GROUP A NEDUNGADI

31 (PDF) DEVCOM ARL FCDD RLA WD L STROHM VA BHAGWANDIN J BRYSON B BURCHETT I CELMINS J DESPIRITO LD FAIRFAX B GRUENWALD J PAUL JD VASILE T. LIANG J SAHU C MERMAGEN FCDD RLA L W OBERLE T SHEPPARD FCDD RLA LB N TRIVEDI FCDD RLA LC J SADLER FCDD RLA LD M MINNICINO A WILLIAMS M NUSCA A MCBAIN FCDD RLA LF M ILG B TOPPER D EVERSON T BROWN FCDD RLA LH R SUMMERS FCDD RLA CL F FRESCONI FCDD RLA V S SILTON FCDD RLA VA L BRAVO A GHOSHAL M MUTHUVEL